https://doi.org/10.5194/egusphere-2026-996
Preprint. Discussion started: 7 April 2026

Instantaneous radiative forcings due to the first indirect effect linked to warm clouds in the Amazon

Andre Cezar Pugliesi[1], Alexandre Lima Correia[2], and Micael Amore Cecchini[1]

[1]Institute of Astronomy, Geophysics and Atmospheric Sciences, USP, São Paulo, Brazil
[2]Institute of Physics, USP, São Paulo, Brazil

Correspondence: Andre Cezar Pugliesi (andre.cezar.silva@gmail.com)

Abstract. Much of the present uncertainty in effective radiative forcing due to aerosol–cloud interactions (ERFaci) arises from aerosol–cloud adjustments. Nevertheless, estimating instantaneous radiative forcing due to aerosol–cloud interactions (IRFaci) remains important because it provides observation-based benchmarks for model evaluation. Such estimates are particularly scarce for warm Amazonian clouds, particularly from approaches combining surface-based remote sensing with in situ aircraft observations. Here, we estimate IRFaci for low-level warm clouds over Amazon using the GoAmazon2014/5 datasets. Cloud microphysical properties were constrained with ground-based remote sensing and in situ measurements, used to configure cloud representations and coupled to libRadtran simulations of daily top-of-atmosphere upward irradiance. To reduce uncertainty in baseline atmosphere, two clean reference states are defined, including one designed to represent the seasonal variability of natural background aerosol conditions. Campaign-mean IRFaci values were -11.8 $\mathrm{W\,m^{-2}}$ (interquartile range: -23.0 to -2.4 $\mathrm{W\,m^{-2}}$) and -1.3 $\mathrm{W\,m^{-2}}$ (-5.8 to 0.3 $\mathrm{W\,m^{-2}}$) for the two reference-state definitions. The first estimate matches the maximum literature IRFaci per AOD unit in Amazon; the second aligns with IPCC's global -0.7 ± 0.5 $\mathrm{W\,m^{-2}}$. Sensitivity tests showed a strong dependence of IRFaci on aerosol load under clean conditions, decreasing with higher loads. Although it does not quantify aerosol–cloud adjustments or ERFaci, this research provides an observationally constrained estimate of IRFaci in the Amazon, serving as a benchmark for future Amazon-focused studies of ERFaci.

1 Introduction

Anthropogenic factors generate disturbances in the global climate system and cause climatic radiative forcings (RF), defined as differences in global net irradiance between a reference atmospheric state and a state perturbed by an external climate agent (IPCC, 2013). The radiative imbalance caused by RF can prompt the atmosphere to seek a new equilibrium through variations in its internal temperature (IPCC, 2013). This re-equilibration can be modulated by the temperature of the oceans and/or continents (Levitus et al., 2012; Trenberth et al., 2014), whether or not adjustments are made to the tropospheric and/or stratospheric temperature profiles (Solomon et al., 2010; Santer et al., 2013). Effective radiative forcings (ERF) are calculated after these profiles have adjusted and reached a new radiative balance. In contrast, instantaneous radiative forcings (IRF) are obtained when no changes in temperature profiles are considered (IPCC, 2013).

Atmospheric aerosols act as cloud condensation nuclei (CCN) and ice nucleation particles (INP), playing a crucial role in cloud formation (Petters and Kreidenweis, 2007). Aerosol–cloud interactions (ACI) influence cloud microphysics (Wang et al., 2024), altering the droplet size distribution (Cecchini et al., 2016), optical properties (Zhao and Garrett, 2015), lifetime (Albrecht, 1989) and precipitation formation (Machado et al., 2018). Consequently, ACIs involving anthropogenic aerosols significantly affect global radiative balance and represent one of the main sources of uncertainty in climate models (Forster et al., 2021). The radiative forcing resulting from ACI (RFaci) can also be categorized as effective (ERFaci) or instantaneous (IRFaci). ERFaci accounts for adjustments in the initial changes in cloud droplet and ice crystal formation rates. These adjustments stem from variations in cloud fraction (f_c), cloud liquid water content (LWC), convective intensity, precipitation efficiency, and cloud lifetime, in addition to cloud formation or suppression in remote areas due to altered atmospheric circulation (Forster et al., 2021). IRFaci corresponds to the increase in cloud optical depth and albedo for a constant LWC. Environments with high aerosol concentrations increase the number of small droplets of clouds, increasing the albedo of the cloud that reflects more radiation to space — a mechanism known as the "cloud albedo effect," the "Twomey effect," or the "first indirect aerosol effect" (Twomey, 1974, 1977).

The estimation of ERFaci and IRFaci on global and regional scales has been the focus of many studies (e.g. Dong and Mace, 2003; Lebsock et al., 2008; Hasekamp et al., 2019; Diamond et al., 2020). The complexity in quantifying RFaci lies mainly in representing the reference atmosphere (Haywood and Boucher, 2000; Hamilton, Lee, Pringle, Reddington, Spracklen, and Carslaw, 2014), especially when the pre-industrial (PI) period is considered (Lee et al., 2016). This representation depends on a set of hypotheses and assumptions, including a degree of arbitrariness (Gryspeerdt et al., 2023) and constitutes an important source of uncertainty (Carslaw et al., 2013). Therefore, a detailed evaluation of the aerosol conditions in the reference state can reduce the uncertainties associated with the RFaci estimates (Gryspeerdt et al., 2023).

Warm clouds are regarded as the main mediators of aerosol radiative forcing through ACI (Heyn et al., 2017; Mülmenstädt and Feingold, 2018). Several studies have used modeling or satellite remote sensing data to quantify and analyze RFaci values associated with warm clouds (e.g. Quaas et al., 2009; Chen et al., 2014; Christensen et al., 2017; Toll et al., 2019), often disregarding continental areas. Among the more regionalized efforts (e.g. Keil and Haywood, 2003; Mace et al., 2006; Marsing et al., 2023; Wang et al., 2023; Herbert and Stier, 2023), only Herbert and Stier (2023) aimed to quantify IRFaci in the Amazon region, also using satellite sensor data. This shows that research on instantaneous forcings due to the Twomey effect in warm clouds over the Amazon rainforest remains limited, particularly when the estimates are derived from in situ or ground-based observations.

This study proposes a new method to estimate IRFaci caused by aerosol pollution in low-level warm clouds in the central Amazon. The IRFaci calculations are based on ground-based and in situ measurements and are performed according to two distinct "clean" reference atmospheric states. We hypothesize that a reference state based on irradiance values that follow the natural seasonal variability of aerosols could reduce the uncertainties in IRFaci estimates. We also assess the sensitivity of warm-cloud IRFaci to different aerosol concentrations in the Amazonian atmosphere.

2 Methodology

2.1 Spatio-temporal domain

The annual cycle of aerosol number concentration in the Amazon is characterized by extreme variations, from 250 particles cm^{-3} during the wet season to values as high as 30,000 particles cm^{-3} in the dry season (Pöschl et al., 2010). This contrast makes the Amazon region a natural laboratory for studying aerosol–cloud interactions. In this study, datasets obtained during the GoAmazon2014/5 campaign (Martin et al., 2016), carried out in 2014 and 2015 in the Brazilian Amazon, were used. The experimental sites of GoAmazon2014/5 were selected based on seasonal timing and the prevailing wind direction. The sites designated as "T0" were located north of the city of Manaus, a region undisturbed by the urban pollution plume due to the prevailing northeasterly winds. The Sites "T1" and "T2" were positioned south of Manaus. The "T3" and "T3u" sites were located southwest of the city, alternately influenced by clean and polluted air masses (Martin et al., 2016) due to variations around the mean wind direction.

In this work, we used data collected from the T3 site (3.2° S, 60.6° W), which accommodated the largest number of instruments during both GoAmazon2014/5 campaign years. At T3, instruments operated by the U.S. Department of Energy (DOE) under the Atmospheric Radiation Measurement Program (ARM, https://www.arm.gov/) were deployed, including the ARM Mobile Facility 1 (AMF-1) and the ARM Mobile Aerosol Observing System (MAOS; (Uin et al., 2019)). Furthermore, during the two intensive operational periods (IOP1 and IOP2, from 1 February to 31, March 2014, and from 15 August to 15, October 2014, respectively) of GoAmazon2014/5, other instrumental platforms were also employed, such as the Gulfstream-159 aircraft ("G1"; (Schmid et al., 2014)) and the HALO aircraft (High Altitude and Long Range Research Aircraft; (Wendisch et al., 2016)). The HALO aircraft flew as part of a collaboration effort with the Brazilian-German project ACRIDICON-CHUVA (Wendisch et al., 2016).

2.2 Ground-based datasets

The atmospheric and cloud properties obtained by ground-based remote sensing included the f_c, the liquid water path (LWP), the cloud base height, and the cloud top height (CBH and CTH, respectively). All datasets were maintained and provided continuously by the ARM program. The data set f_c originated from a Value-Added Product (VAP; (Riihimaki et al., 2019)) that combined measurements from different radiometers to derive total, direct and diffuse shortwave and longwave downward and upward irradiances, as well as f_c for shortwave (Long et al., 2006) and longwave (Dürr and Philipona, 2004) radiation. The f_c values were retrieved at one-minute intervals and did not distinguish between different types of cloud.

The LWP values were also derived through an algorithm (Turner et al., 2007) that combines atmospheric thermodynamic state information — vertical profiles of air temperature, pressure, and relative humidity — with brightness temperature measurements at 23.8 GHz and 31.4 GHz obtained by a surface-based microwave radiometer (MWR). As in f_c, the base and top heights of the observed cloud layers were derived from a VAP (Kollias et al., 2007) that combined measurements from a W-band ARM Cloud Radar (WACR, operating at 95.04 GHz) and a micropulse lidar system (MPL), with CBH and CTH values sampled every 5 seconds.

The total aerosol scattering coefficient ($\beta_{sct.}$), the total concentration of organic mass ("Total Organics" or "Org."), the number concentration of cloud condensation nuclei (CCN) and the spectral aerosol optical depth (AOD) were among the aerosol properties analyzed. The values of $\beta_{sct.}$ were derived (Uin, 2024) using a pair of nephelometers measuring $\beta_{sct.}$ as a function of relative humidity at intervals of one-min, at three wavelengths λ (700, 550 and 450 nm), and for two cuts in particle size (1 $\mu\mathrm{m}$ and 10 $\mu\mathrm{m}$). The values of Total Organics were obtained using an Aerosol Chemical Speciation Monitor (ACSM), a mass spectrometer based on thermal vaporization and subsequent ionization of aerosol particles smaller than 1 $\mu\mathrm{m}$ (Watson, 2017).

The CCN number concentrations at the T3 site were measured using a cloud condensation nuclei particle counter (CCNC). This instrument measures aerosol concentrations by sampling air through a column with thermodynamically unstable supersaturated water vapor, which can condense on aerosol particles. The resulting grown particles are counted and sized by an Optical Particle Counter (OPC). Thus, CCNC quantifies the number concentration of particles activated as a function of the instrument's internal supersaturation (Uin and Enekwizu, 2024).

Spectral AOD values constituted the final aerosol-related variable used in this study. Due to the limited availability of samples, two complementary datasets were employed. The first was obtained from a sun photometer belonging to AERONET (AErosol RObotic NETwork; https://aeronet.gsfc.nasa.gov/), an instrument equipped with a 25 cm collimator system mounted on a robotic base that can be programmed to point either toward the sky or directly at the Sun. This photometer measures spectral solar and sky radiances at eight wavelengths (340, 380, 440, 500, 675, 870, 1020, and 1640 nm) and uses them to calculate AOD values and other quantities (Giles et al., 2019), after correcting for molecular scattering and absorption caused by ozone and other atmospheric gases. The AERONET-derived AOD values used here correspond to the 500 nm wavelength, being measured at variable sampling rates (ranging from 1.9 to 551.3 minutes).

This data set was complemented with AOD values retrieved from solar irradiance measurements acquired by a MultiFilter Rotating Shadowband Radiometer (MFRSR) operated by ARM. These irradiances serve as input for a VAP that applies the algorithms described by Harrison and Michalsky (1994), Michalsky et al. (2001), and Alexandrov et al. (2004) to derive spectral AOD values at six wavelengths (415, 500, 615, 673, 870, and 940 nm), with a sampling interval of 20 seconds.

2.3 In situ datasets

In situ measurements of the liquid water content in clouds, total water content (TWC), total cloud droplet concentration (N_d), cloud droplet size distribution (N(D)), and effective cloud droplet diameter ($D_{eff.}$) were performed using instruments onboard the G-1 and HALO aircraft.

Of the 35 flights conducted by the G-1 during IOP 1 and IOP 2, 32 flew over the T3 site and were used in this study. Measurements of LWC and TWC were carried out using the WCM-2000 instrument, a sensor composed of a scoop-shaped device equipped with several heated wires. Some of these wires are directly exposed to the airflow and cloud water droplets, while a separate reference wire is exposed only to the airflow. A power control system maintains constant voltage in one wire and constant temperature in the others. In the case of constant temperature operation, the "King-type" probe (King et al., 1978) uses the system's power values, relative airspeed, ambient temperature, individual wire dimensions, and the latent heat of water vaporization to calculate LWC and TWC each second (for calculation details, see the user manual available at https://www.scieng.com/pdf/WCM2000User.pdf).

The N_d and N(D) values measured during the G-1 flights were obtained using the Fast Cloud Droplet Probe (FCDP; manual available at http://www.specinc.com/node/123), an instrument that employs a focused laser beam to size hydrometeors based on the amount of scattered light during particle–beam interaction. The FCDP has a resolution of 3 µm, measures droplet diameters between 1 and 50 µm, and divides them into 20 equally spaced size bins.

The HALO aircraft conducted 14 research flights between September and October 2014, during the GoAmazon2014/5 IOP 2. The flights were designed to cover five distinct mission types, focusing on different processes involving clouds, aerosols, chemistry, and radiation (Wendisch et al., 2016). The flights were numbered chronologically as ACXX, with X ranging from 07 to 20. Among these, only two flew over densely forested areas to the north and northwest of Manaus (AC09 and AC18, conducted on 11 September and 28 September, 2014, respectively) and are used here. Those flights were selected to serve as the background reference because the clouds measured were not directly affected by biomass-burning aerosols.

LWC and D_{eff} measurements were obtained using the Cloud and Aerosol Spectrometer with Detector for Polarization (CAS-DPOL), a spectrometer that also measures the cloud droplet size distribution from 0.5 to 50 µm (Wendisch et al., 2016). Filtering of LWC and D_{eff} for warm clouds was performed using flight altitude data (above sea level, ASL) from the Basic HALO Measurement and Sensor System (BAHAMAS), considering a maximum flight height of 3 km.

Table 1 compiles the atmospheric, cloud, and aerosol variables used in this study. The table also shows the corresponding instrument, measurement unit, experimental platform, and sampling interval for each variable. For CBH, CTH, and LWP, 1-minute averages were calculated to facilitate the derivation of microphysical parameters for subsequent warm-cloud modeling. For AOD, $\beta_{sct.}$, Total Organics, CCN, and f_c, daily and/or diurnal averages were calculated. The mathematical formulations of the variables presented in Table 1 are provided in Sect. 2.4.

2.4 Clean and polluted scenarios

Periods with lower and higher average aerosol number concentration during the GoAmazon2014/5 campaign will be referred to as “clean” and “polluted” scenarios, respectively. The term “clean” does not imply a complete absence of anthropogenic aerosols in the atmosphere, but rather a distinctly lower concentration compared to the “polluted” scenario. The latter corresponds to episodes in 2014 and 2015 with a higher frequency of biomass-burning events and advection of the Manaus pollution plume over the T3 site.

The identification of clean and polluted scenarios during GoAmazon2014/5 was based on a manual analysis of daily means of $\beta_{sct.}$, Org., CCN, and AOD. Among these quantities, $\beta_{sct.}$ and AOD are directly proportional to aerosol loading and result from the interaction between aerosols and incident electromagnetic radiation, particularly at wavelengths between approximately 0.3 µm and 4 µm — the solar spectrum range. This interaction is described by Mie scattering (Mie, 1908), which applies Maxwell’s electromagnetic theory to describe radiation scattered by spherical particles with radius r comparable to or greater than the incident wavelength. Macroscopically, $\beta_{sct.}$ at position s' along an optical path s for aerosols with refractive index $n(\lambda)$ is given by Eq. (1), where $N_p(r, s')$ is the number of aerosol particles per unit air volume per size interval at position s', and $Q_{sct.}$

Table 1. Cloud and aerosol properties used in this work.

Variable	Unit	Instrument	Platform	Sampling interval	Observation
LWC	$\mathrm{g\,m^{-3}}$	WCM-2000	G-1	1 second	IOP 1 and 2
LWC	$\mathrm{g\,m^{-3}}$	CAS-DPOL	HALO	1 second	IOP 2
TWC	$\mathrm{g\,m^{-3}}$	WCM-2000	G-1	1 second	IOP 1 and 2
N_d	$\mathrm{drops\,L^{-1}}$	FCDP	G-1	1 second	IOP 1 and 2
$N(D)$	$\mathrm{drops\,L^{-1}\,\mu m^{-1}}$	FCDP	G-1	1 second	IOP 1 and 2
D_{eff}	μm	CAS-DPOL	HALO	1 second	IOP 2
Altitude	m ASL	BAHAMAS	HALO	1 second	IOP 2
CBH	m AGL	WACR + MPL	Ground	5 seconds	2014–2015
CTH	m AGL	WACR + MPL	Ground	5 seconds	2014–2015
LWP	$\mathrm{g\,m^{-2}}$	MWR	Ground	20 seconds	2014–2015
f_c	%	Radiometers	Ground	1 minute	Shortwave; 2014–2015
AOD	unitless	AERONET	Ground	Variable	550 nm; 2014–2015
AOD	unitless	MFRSR	Ground	20 seconds	500 nm; 2014–2015
$\beta_{\mathrm{sct.}}$	$\mathrm{Mm^{-1}}$	Nephelometer (NEPH3W)	Ground	1 minute	500 nm; 1 μm cut; 2014–2015
Total organics (Org.)	$\mathrm{\mu g\,m^{-3}}$	ACSM	Ground	1 minute	∼50–700 nm; 2014–2015
CCN	$\mathrm{particles\,cm^{-3}}$	CCNC	Ground	1 minute	2014–2015

is the scattering efficiency factor. Spectral AOD is related to the amount of optically active aerosols in the atmospheric column. To derive it, one must consider the solar zenith angle (θ_0 or SZA, formed between the vertical direction and the propagation 160 path of the incident radiation beam) and the linear absorption coefficient $\beta_{abs.}$ (Eq. (2)), resulting in the formulation shown in Eq. (3).

$$\beta_{\mathrm{sct.}}(\lambda, s') = \pi r^2 Q_{\mathrm{sct.}}\left[\frac{2\pi r}{\lambda}, n(\lambda)\right]\int_0^\infty N_p(r,s')\,dr \qquad (1)$$

$$\beta_{\mathrm{abs.}}(\lambda, s') = \pi r^2 Q_{\mathrm{abs.}}\left[\frac{2\pi r}{\lambda}, n(\lambda)\right]\int_0^\infty N_p(r,s')\,dr \qquad (2)$$

$$\mathrm{AOD}(\lambda) = \int_0^s \left[\beta_{\mathrm{sct.}}(\lambda,s) + \beta_{\mathrm{abs.}}(\lambda,s)\right]\cos(\theta_0)\,ds \qquad (3)$$

165 Daily means of $\beta_{sct.}$, Org., and CCN for 2014 are displayed in Fig. 1. The period between days 10 and 90 of 2014 was selected as representative of the clean scenario, whereas the intervals between days 210–277 and 300–345 were chosen to represent polluted periods. For 2015, the same procedure was applied to the daily time series of $\beta_{sct.}$, Org., and AOD. Figure

https://doi.org/10.5194/egusphere-2026-996
Preprint. Discussion started: 7 April 2026

2, which presents these series, shows that aerosol influence peaked during the second half of the year. During the polluted period of 2015, the $\beta_{sct.}$ and Org. peaks were greater than those observed in 2014, which exhibited a shorter clean period compared to 2015. From the time series shown in Figs. 1 and 2, the start and end days of the clean and polluted scenarios for 2014 and 2015 were determined. Table 2 summarizes these intervals and the weighted means of $\beta_{sct.}$, Org., CCN, and AOD calculated for them. This reference will be extensively used in the calculation and analysis of IRFaci.

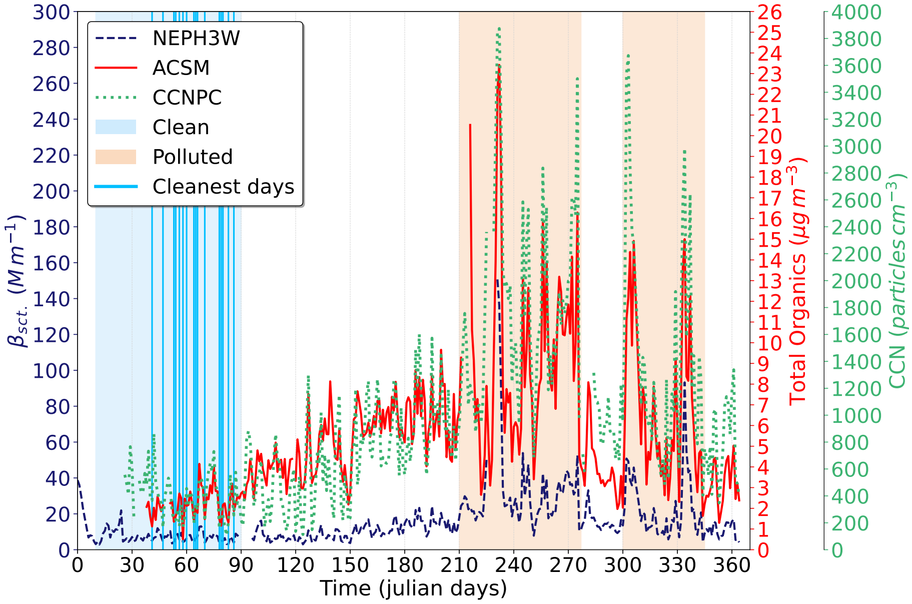

Figure 1. Daily averages of $\beta_{sct.}$, Org. and CCN for 2014. The legend indicates the instruments responsible for data acquisition and the days that demilit the clean and polluted scenarios. The identification of cleanest days within the clean scenario was carried out using a clustering technique described in Sect. 2.4.

Table 2. Days that define the clean and polluted scenarios for 2014 and 2015. The values in parentheses are the weighted means of $\beta_{sct.}$, Org. and CCN (for 2014, respectively) and of $\beta_{sct.}$, Org. and AOD from AERONET (for 2015, respectively) calculated for the corresponding interval.

Year	Clean	Polluted 1	Polluted 2
2014	Jan. 11th to Apr. 1st (7.7, 2.3, 400.2)	July 30th to Oct. 5th (30.8, 9.1, 1748.5)	Oct. 28th to Dec. 12th (22.4, 6.8, 1411.8)
2015	Jan. 1st to July 30th (6.7, 2.9, 0.1)	Sep. 23th to Nov. 30th (104.9, 28.8, 0.6)	—

The clean scenarios of 2014 and 2015 define the periods within which the cleanest days were used as the basis for the determination of the first atmospheric reference state. The selection of these cleanest days proceeded as follows: first, all days sharing common data for the variables $\beta_{sct.}$, Org., CCN, and AOD (for AOD, since the AERONET dataset had many empty data points, only data derived from the MFRSR were considered) were identified. For these days, daytime medians (06:00–18:00 LT) were

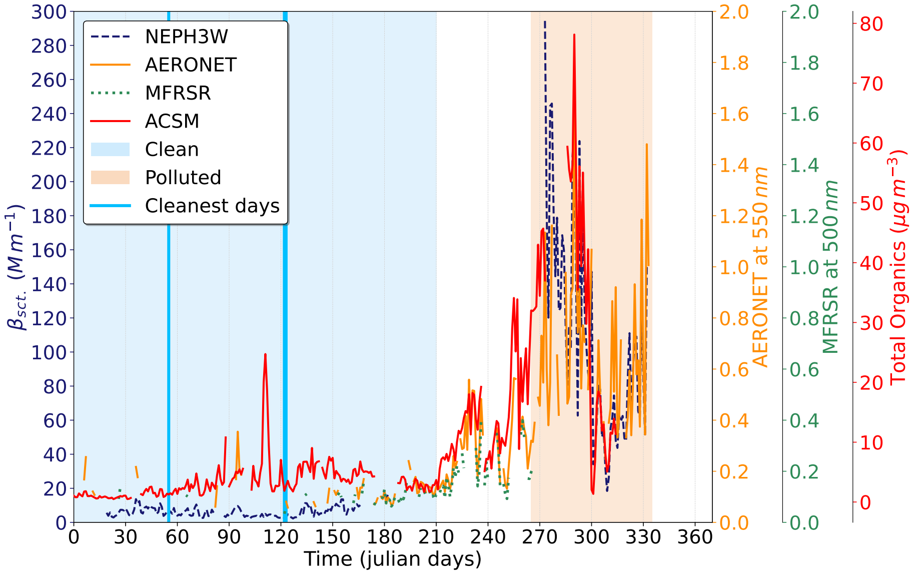

Figure 2. Daily averages of $\beta_{sct.}$, AOD and Org. for 2015.

calculated for each of the four variables. After normalizing these medians, the K-Means clustering algorithm (Lloyd, 1982) was applied using 2, 3, and 4 clusters. For each cluster and each variable, a characteristic median was assigned. Comparing the medians across different cluster counts helped determine the optimal number of clusters, corresponding to cases in which no overlap occurred between the characteristic medians of distinct groups.

From the identification of optimal cluster counts for 2014 and 2015, the minimum characteristic median values were obtained, allowing the identification of the cleanest days within each clean scenario. For 2014, six days in February (11, 17, 23, 24, 26, and 28) and ten in March (2, 6, 7, 8, 12, 20, 21, 22, 25, and 28) were selected. For 2015, the cleanest days were 25 February and 3–4 May. The mean upward irradiance values at the top of the atmosphere (TOA) simulated for these days were later used as a fixed reference for the IRFaci calculations.

2.5 Extension of $D_{eff.}$ and LWC measurements for the GoAmazon2014/5 period

Upward irradiance values at the TOA were obtained using the libRadtran radiative transfer code (Emde et al., 2016), which simulated warm clouds modeled from LWC values (Eq. (4); (Morrison et al., 2005)), where ρ is the liquid water density, r is the cloud droplet radius, N(D) is given by Eq. (5), and $r_{eff.}$ by Eq. (6a) (Stephens, 1978). However, experimental in situ values of LWC, TWC, N(D), N_d, and $D_{eff.} = 2\, r_{eff.}$ were obtained only during G-1 flights, limiting the temporal coverage of these datasets. The procedure used to extend their availability consisted of:

1. Deriving empirical relationships between the in situ measured LWC and $r_{eff.}$ values;

2. Using surface-based datasets of CBH, CTH, and LWP to calculate LWC_{ground} = LWP/(CTH-CBH);

3. Inserting LWC_{ground} values into the empirical relationships obtained in the first step to extrapolate $\text{r}_{eff.}$ for the entire GoAmazon2014/5 campaign period.

The first step in obtaining empirical relationships between LWC and $\text{r}_{eff.}$ was to consider only positive simultaneous measurements of N_d and LWC, ensuring that the aircraft was within a cloud. Subsequently, only cases with zero ice water content (IWC, equals the mathematical difference between TWC and LWC) were retained, thereby filtering warm clouds. During data screening, cases where $\text{N}_d < 0.3$ particles cm^{-3} and $\text{LWC} < 0.02\ \text{g}\,\text{m}^{-3}$ were excluded, removing experimental points associated with fog or extremely tenuous clouds. Finally, $\text{r}_{eff.}$ was computed according to Eq. (6b), where $<\text{r}_j>$ represents the j-th mean of one of the 20 size intervals (bins) in which N(D) values were classified.

$$\text{LWC} = \frac{4\pi}{3}\rho \int\limits_{0}^{\infty} r^3 N(D)\,dr \tag{4}$$

$$N(D) = N_0\, r^m e^{-\Lambda r} \tag{5}$$

$$r_{\text{eff.}} = \frac{\int_0^\infty r^3 N(D)\,dr}{\int_0^\infty r^2 N(D)\,dr} \tag{6a}$$

$$r_{\text{eff.}} = \frac{\sum_{j=1}^{20} < r_j >^3 N(D)_j\,dr}{\sum_{j=1}^{20} < r_j >^2 N(D)_j\,dr} \tag{6b}$$

The scatterplot of $\text{r}_{eff.}$ versus LWC for IOP 1 did not exhibit patterns that could be easily fitted by simple functions (e.g., linear or quadratic). Consequently, the data were divided into 20 equally spaced LWC bins (with a width of $0.05\ \text{g}\,\text{m}^{-3}$, between 0.02 and $1.02\ \text{g}\,\text{m}^{-3}$), within which LWC and $\text{r}_{eff.}$ medians were calculated. Similarly to this study, Reid et al. (1999) explored the relationship between LWC and $\text{r}_{eff.}$ of warm clouds over the Brazilian Amazon. Those authors used in situ aircraft measurements focusing on warm stratiform and cumuliform clouds with bases located within the planetary boundary layer. Their datasets, obtained between August and September 1995 — when the Amazonian atmosphere is typically affected by smoke and biomass-burning aerosols — produced $\text{r}_{eff.}$–LWC distributions for cumulus and stratocumulus clouds that closely resembled those observed here for IOP 1.

For IOP 2, the LWC/N_d ratios were considered instead of LWC alone. These ratios were then applied to Eqs. (7) and (8), corresponding to cumulus and stratocumulus clouds, respectively (Reid et al., 1999). In their analysis, Reid et al. (1999) concluded that, after testing several fitting functions, the hyperbolic arccosine function provided the best fit — motivating its adoption here to adjust the median pairs for IOPs 1 and 2 (Fig. 3).

$$r_{\text{eff.}} = 6.67\left(\frac{LWC}{N_{\text{d}}}\right)^{0.31} \tag{7}$$

220 $$r_{\text{eff.}} = 7.50\left(\frac{LWC}{N_{\text{d}}}\right)^{0.33} \tag{8}$$

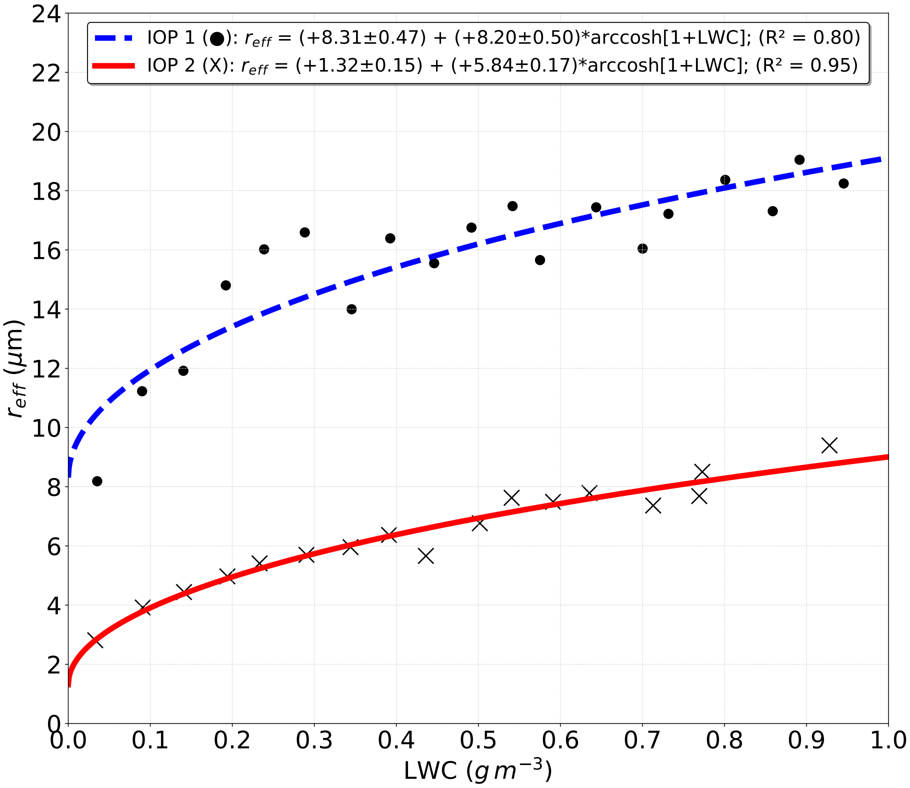

Figure 3. Dispersion of medians of $r_{eff.}$ and LWC calculated in the 20 bins for IOP 1 and 2. The adjustments (hyperbolic arc cosine function) originated the equations shown in the graph's legend.

Following the procedure to extend the dataset coverage, surface-derived values of CBH, CTH, and LWP were used to compute LWC_{ground}. These LWC_{ground} values were then inserted into the empirical relationships shown in Fig. 3, generating new $r_{eff.}$ estimates for warm clouds during IOPs 1 and 2. This procedure enabled the construction of an expanded database, covering all days within the clean and polluted periods defined by the intervals listed in Table 2, thereby increasing data availability across 2014 and 2015. 225

For transition periods, hybrid adjustments were made using weighted averages that combined both empirical functions. For instance, during the first transitional days of 2014, the computed $r_{eff.}$ values had a greater weight from the clean-period equation, while the last days were progressively influenced by the polluted-period function. This approach enabled the generation of $r_{eff.}$ values as a function of LWC_{ground} for nearly every day of the GoAmazon2014/5 campaign, consequently allowing the modeling of warm clouds for almost the entire observation period.

2.6 Configuration of Warm Cloud Models

Selection of warm clouds was also performed through filtering of the LWC_{ground} and CTH datasets. The interval [0.2–0.4] $g\,m^{-3}$ for LWC_{ground} encompasses typical values of cumulus and stratiform clouds in both clean and polluted continental environments (Hess et al., 1998), and was therefore applied as a filter to the LWC_{ground} data. Additionally, only clouds with CTH less than or equal to 3 km were considered to ensure that the final results represented warm clouds exclusively.

The effective radius of liquid clouds increases with altitude in the atmosphere (Martins et al., 2011; Rosenfeld and Woodley, 2003), and this behavior was adopted as the conceptual model to simulate characteristic warm clouds for each day of the GoAmazon2014/5. To represent the vertical increase of $r_{eff.}$ with altitude, the clouds were configured with two horizontal layers, ensuring that the $r_{eff.}$ and LWC values in the models were higher in the upper layer. The base height of the modeled clouds was set according to the 12.5th percentile of CBH values, while the top height corresponded to the 87.5th percentile of the CTH data distribution. The central height was defined as the arithmetic mean between the base and top heights. The 12.5th and 87.5th percentiles of the daily $r_{eff.}$ and LWC_{ground} distributions were similarly selected to describe the $r_{eff.}$ and LWC values at the base and top, respectively, while the middle layer was represented by the median of the same distributions. Table 3 summarizes the statistical parameters used to simulate representative warm clouds for most days of the GoAmazon2014/5 campaign.

Table 3. Configuration of "daily" clouds. The statistics shown were calculated from daily distributions of LWC_{ground} (equals the ratio between LWP and CTH-CBH difference) and of the corresponding $r_{eff.}$, wich was calculated from adjusted equations shown in Fig. 3.

Cloud region	Height (km)	LWC ($g\,m^{-3}$)	$r_{eff.}$ (μm)
Top	CTH 87.5th percentile	87.5 percentile	87.5 percentile
Center	Mean between base and top	50.0 percentile	50.0 percentile
Base	CBH 12.5th percentile	12.5 percentile	12.5 percentile

2.7 Radiative transfer code configuration to obtain upward irradiance at TOA

The integrated upward irradiance values (hereafter referred to as F) at the TOA were obtained using the libRadtran radiative transfer model, which applies the DISORT method (DIScrete Ordinate Radiative Transfer solver; Stamnes et al. (1988)) to solve the radiative transfer equation after accounting for adjustments to atmospheric boundary conditions. In addition, libRadtran uses the "medium" spectral resolution mode (bandwidth = $5\,cm^{-1}$) of the REPTRAN parameterization (Gasteiger et al., 2014) as the standard spectral configuration. The wavelength interval selected for the simulations ranged from 300 to 1000 nm, encompassing the entire visible spectrum and a small portion of the near-infrared region. The solar spectrum used extended from 250 to 10,000 nm, with a resolution of 0.1 nm.

https://doi.org/10.5194/egusphere-2026-996
Preprint. Discussion started: 7 April 2026

REPTRAN is also the default method employed by libRadtran to represent atmospheric molecular scattering, applicable to both the solar and terrestrial spectra. For this, vertical profiles of the main atmospheric gases (O_2, O_3, NO_2, CO_2, and water vapor) must be provided. The "standard tropical atmosphere" file available in libRadtran already includes vertical profiles for these gases, along with profiles of air density, temperature, and pressure. The profiles of less abundant trace gases such as N_2O, CO, and CH_4 were taken from the "standard U.S. atmosphere" dataset. Considering this, the tropical atmosphere data provided by the Earth Observation Data Group (EODG) of the University of Oxford (http://eodg.atm.ox.ac.uk/RFM/atm/minor.atm) were used here to generate new vertical profiles for these gases.

The files used to simulate the representative daily warm clouds considered the exact geographic location and elevation of the T3 site. Since T3 was situated in a forested region, a surface albedo of 14% was adopted. The mean CO_2 mixing ratios estimated for 2014 and 2015 according to the Keeling curve (Keeling et al., 2017) were also incorporated. All simulations were configured to represent upward irradiance at TOA for 16:00 UTC (12:00 LT), ensuring that the Sun was near zenith at the simulation time. Moreover, the f_c was set to 100% for all simulations, assuming that the simulated stratiform warm clouds completely covered the sky at 12:00 LT.

2.8 IRFaci estimates for the two clean atmospheric reference states

The upward integrated irradiance values at the TOA obtained from libRadtran (hereafter $F_{libRadtran}$) do not account for variations in the Earth–Sun distance (d). The necessary correction was made using Eq. (9), which assumes a plane-parallel atmosphere. The values of d and the solar zenith angle (θ_0) used in Eq. (9) were calculated using spreadsheets provided by NOAA's Earth System Research Laboratories (https://gml.noaa.gov/grad/solcalc/calcdetails.html). These spreadsheets compute various astronomical parameters for any location on Earth; therefore, the d and θ_0 data were obtained specifically for the T3 site. With these parameters and the $F_{libRadtran}$ outputs, the corrected irradiance values ($F_{corr.}$) were computed, accounting for temporal variations in d throughout 2014 and 2015 at T3.

$$\mathrm{F}_{\mathrm{corr.}} = \frac{d^2 F_{libRadtran}}{cos(\theta_0)} \tag{9}$$

Instantaneous radiative forcings (IRF) were then calculated as the difference between $F_{corr.}$ in the reference state and $F_{corr.}$ in the anthropogenically perturbed state (Eq. (10)). Moreover, since the IRF calculations were based on integrated irradiances simulated for 12:00 LT at T3, the estimation of daily radiative forcing (IRF_{daily}, corresponding to 00:00 to 23:59) required consideration of the variation of the θ_0 throughout the day. This correction was implemented using Eq. 11, which incorporated 120 values of θ_0 sampled every 6 minutes during daylight hours. Because T3 is located near the Equator, the durations of daytime and nighttime were considered nearly identical, and the morning and afternoon periods were approximately equal in length. For this reason, IRF_{daily} corresponds to either the morning or afternoon interval, justifying the division by 2 in Eq. (11).

$$\mathrm{IRF} = F_{\mathrm{corr}}^{\mathrm{reference}} - F_{\mathrm{corr}}^{\mathrm{perturbed}} \tag{10}$$

$$\mathrm{IRF}_{\mathrm{daily}} = \frac{1}{2}\,\frac{\mathrm{IRF}\sum_{n=06:00}^{18:00}\cos(\theta_0)_n}{120} \tag{11}$$

As previously discussed, two clean atmospheric reference values were used in Eq. (10). The first, a fixed value of 689.9 $\mathrm{W\,m^{-2}}$, corresponds to the mean of the corrected irradiances obtained from the cleanest days of the GoAmazon2014/5 campaign. This reference represents natural background atmospheric conditions during the 19 cleanest days of 2014 and 2015, which may differ from those characterizing the polluted periods of the same years. To account for seasonal variability in cloud microphysical properties, a second reference with variable irradiance was implemented. This approach involved generating warm-cloud models (example shown in Table 4) based on LWC data (within the [0.2–0.4] $\mathrm{g\,m^{-3}}$ interval) and $\mathrm{r}_{eff.}$ values corresponding to the cleanest conditions identified during IOP 2. The measurements used originated from HALO aircraft flights AC09 and AC18.

For these models, libRadtran simulated upward integrated irradiances at TOA for θ_0 = 0 and an Earth–Sun distance of 1 AU. The resulting irradiances, 766.7 $\mathrm{W\,m^{-2}}$ and 769.1 $\mathrm{W\,m^{-2}}$, yielded a mean value of 767.9 $\mathrm{W\,m^{-2}}$, which was considered representative of the cleanest possible atmospheric conditions for September 2014. This mean was used as the reference for IRF calculations only during the polluted periods of 2014 and 2015. For the transitional days, reference irradiances were calculated to vary linearly (Fig. 4) between the clean and polluted reference values (689.9 $\mathrm{W\,m^{-2}}$ and 767.9 $\mathrm{W\,m^{-2}}$, respectively). This second approach allowed the computation of new daily forcing values less affected by the seasonal variability of natural atmospheric conditions over the T3 region.

Table 4. Cloud configuration representing 11 September 2014 (AC09), considered one of the two "cleanest" days during IOP 2. The corresponding intervals of LWC ($\mathrm{r}_{eff.}$) for 28 September 2014 were 0.00 to 0.24 $\mathrm{g\,m^{-3}}$ (0.00 to 5.48 μm), 0.24 to 0.27 $\mathrm{g\,m^{-3}}$ (5.48 to 8.03 μm), and 0.27 to 0.00 $\mathrm{g\,m^{-3}}$ (8.03 to 0.00 μm) for base, center, and top portions, respectively. The average LWC and $\mathrm{r}_{eff.}$ values for these two days were 0.26 $\mathrm{g\,m^{-3}}$ and 6.89 μm, respectively. The zero extremes in cloud configuration are necessary for libRadtran to correctly simulate the boundaries of the modeled clouds.

Cloud region	Height (km)	LWC ($\mathrm{g\,m^{-3}}$)	$\mathrm{r}_{eff.}$ (μm)
Top	2 to 3	0.28 to 0.00	8.30 to 0.00
Center	1 to 2	0.26 to 0.28	6.09 to 8.30
Base	0 to 1	0.00 to 0.26	0.00 to 6.09

https://doi.org/10.5194/egusphere-2026-996
Preprint. Discussion started: 7 April 2026

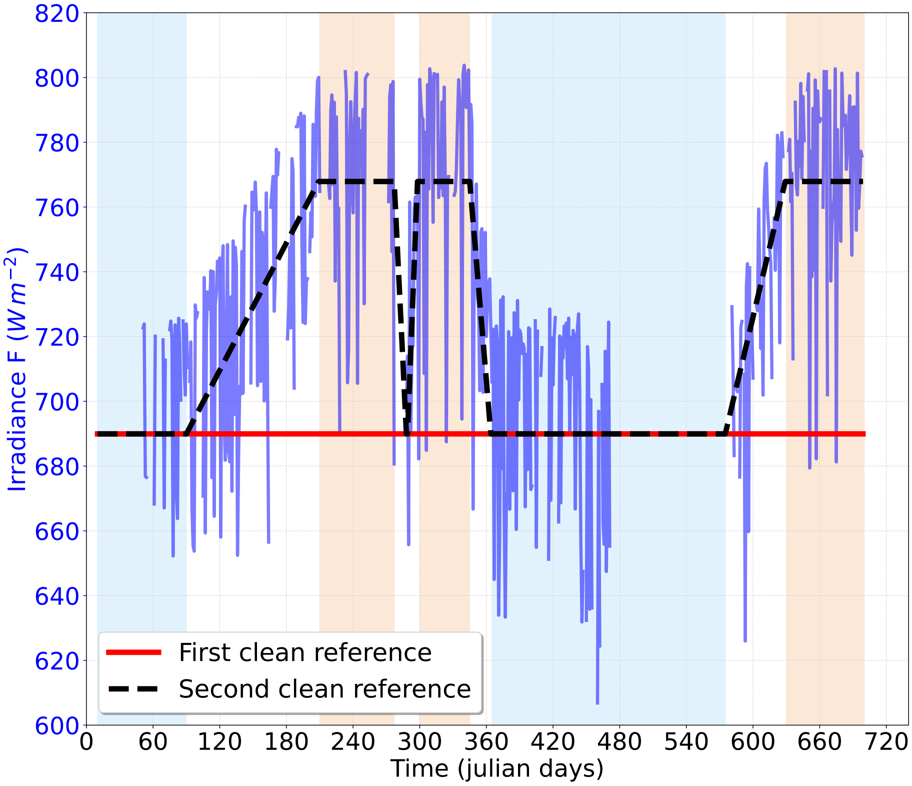

Figure 4. Integrated and corrected upward irradiances ($F_{corr.}$) at TOA for 2014 and 2015 (bluish line varying over the day of the year). The values were calculated for each day and correspond to local solar noon at the T3 site. They are also unaffected by Earth's orbital variation, so the variation over the years is due to changes in the cloud properties. The areas highlighted in blue (brown) represent the clear (polluted) periods for the two years. Days that do not show F values contain incomplete datasets (CBH, CTH, or LWP), making warm cloud modeling impossible. The solid (dashed) red (black) line corresponds to the F value used as a fixed (variable) reference to obtain the IRFaci estimates.

3 Results

3.1 First clean state - "Fixed" irradiance reference

The IRF_{daily} values were obtained assuming a cloud fraction of 100%. However, to regionalize the results according to the actual cloudiness observed at T3, each daily value was also multiplied by the corresponding daytime mean f_c for that specific day. Figure 5, which presents the IRF_{daily} values for the first clean-atmosphere reference, shows that the results incorporating the f_c measured at T3 generally display smaller absolute magnitudes compared to those associated with f_c = 100%. The observed daily oscillation arises from the way the warm-cloud models were configured — that is, based on the percentiles and medians of $r_{eff.}$ and LWC. Figure 5 also clearly reveals the mean reduction in IRF_{daily} magnitude as the more polluted periods approach, with values becoming increasingly negative during those episodes.

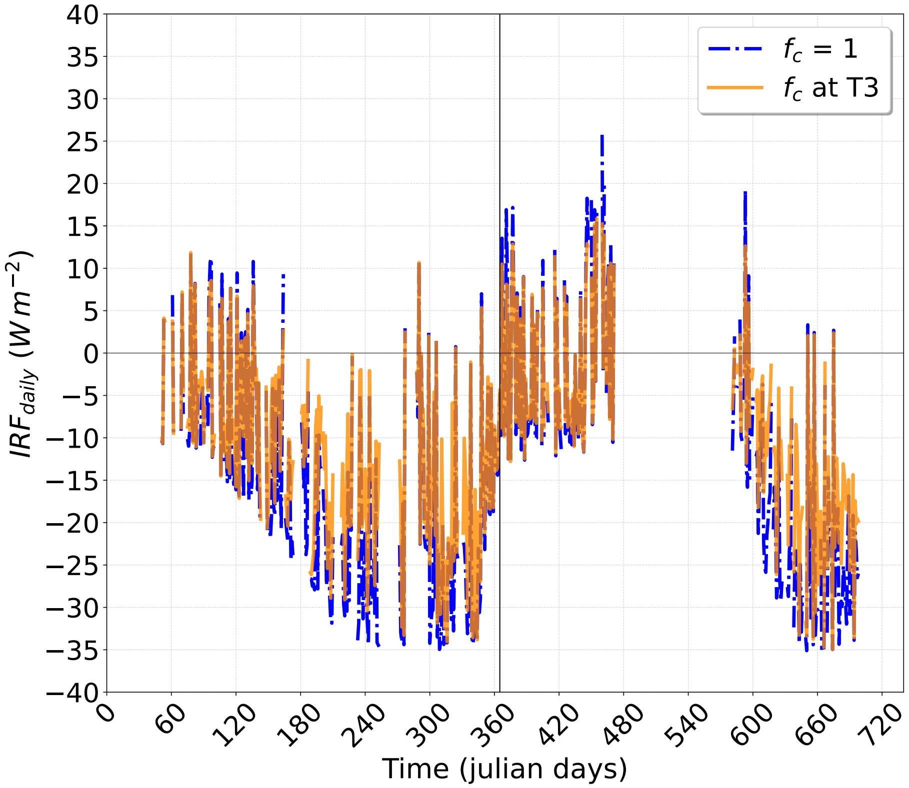

Figure 5. IRF$_{daily}$ values are calculated based on the fixed clean atmosphere reference for 2014 and 2015. Blue line (f$_c$ = 1) indicates the results for an f$_c$ of 100%, while the gold line shows the values according to the f$_c$ measured at T3.

To evaluate the relative behavior of IRF$_{daily}$ values across different aerosol-loading scenarios, boxplots were generated for each case. Figure 6 displays the results for 2014, along with the means and medians for each scenario. Overall, IRF$_{daily}$ values that do not account for the measured f$_c$ at T3 exhibit distributions shifted toward more negative values compared to those incorporating f$_c$ variability, indicating that a constant f$_c$ = 100% produces markedly stronger negative instantaneous radiative forcings. The statistics show progressively more negative values as the clean days give way to polluted ones, with results for the second 2014 transition period showing an increasing trend consistent with the decreasing aerosol parameters displayed in Fig. 1. It is also noteworthy that, although positive values occur only under the clean scenario (at the upper limit of the seventy-fifth percentile), both the means and medians for all scenarios remain negative.

The IRF$_{daily}$ values computed for the polluted period of 2015 (Fig. 7) exhibit means, medians, and percentiles that are more negative than those of the clean and transitional periods of the same year. While mean and median values range from 0 to -8 $\mathrm{W\,m^{-2}}$ during the clean period, the values associated with the polluted scenario lie between approximately -15 and -30 $\mathrm{W\,m^{-2}}$. An important observation is that the mean IRF$_{daily}$ values for f$_c$ = 1 and for the measured cloud fraction at T3 are nearly identical under cleaner atmospheric conditions, which is not the case for the polluted scenario. This is noteworthy

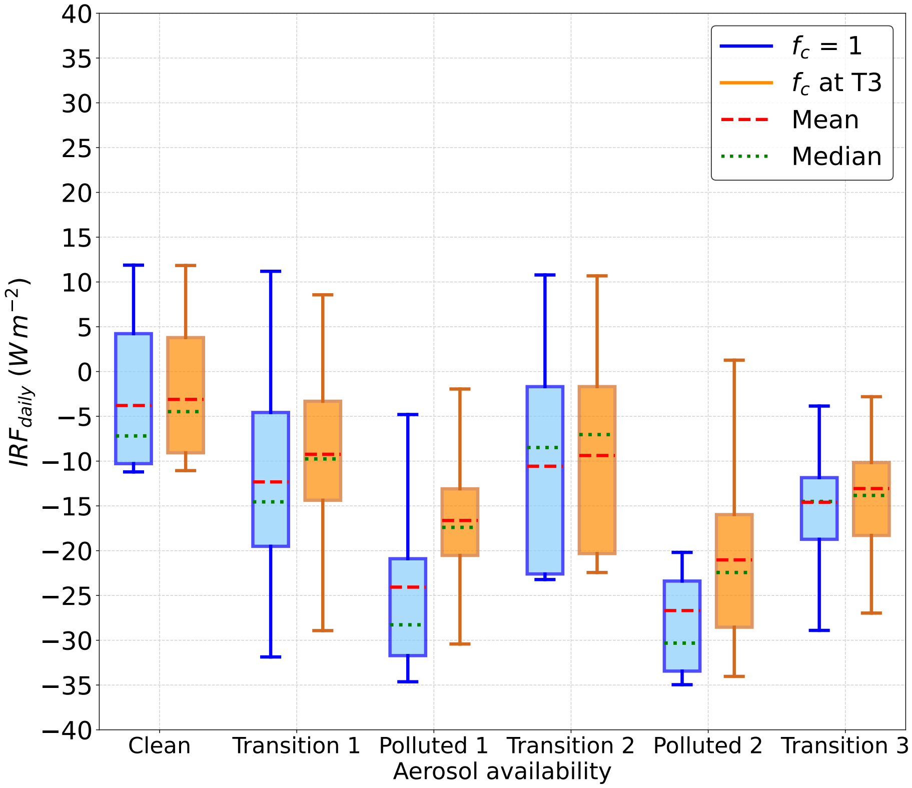

Figure 6. Boxplots, means and medians of IRF_{daily} calculated according to the first clean atmosphere reference for 2014 and separated according to the different aerosol availability at T3. The polluted period was divided into two subintervals due to the significant drop in concentrations of $\beta_{sct.}$, Org. and CCN shown in Fig. 1.

because—even with elevated aerosol concentrations and reduced cloud cover during polluted periods—the instantaneous radiative forcing associated with the few existing clouds is more negative than that produced by the more numerous clouds in the clean season. 325

https://doi.org/10.5194/egusphere-2026-996
Preprint. Discussion started: 7 April 2026

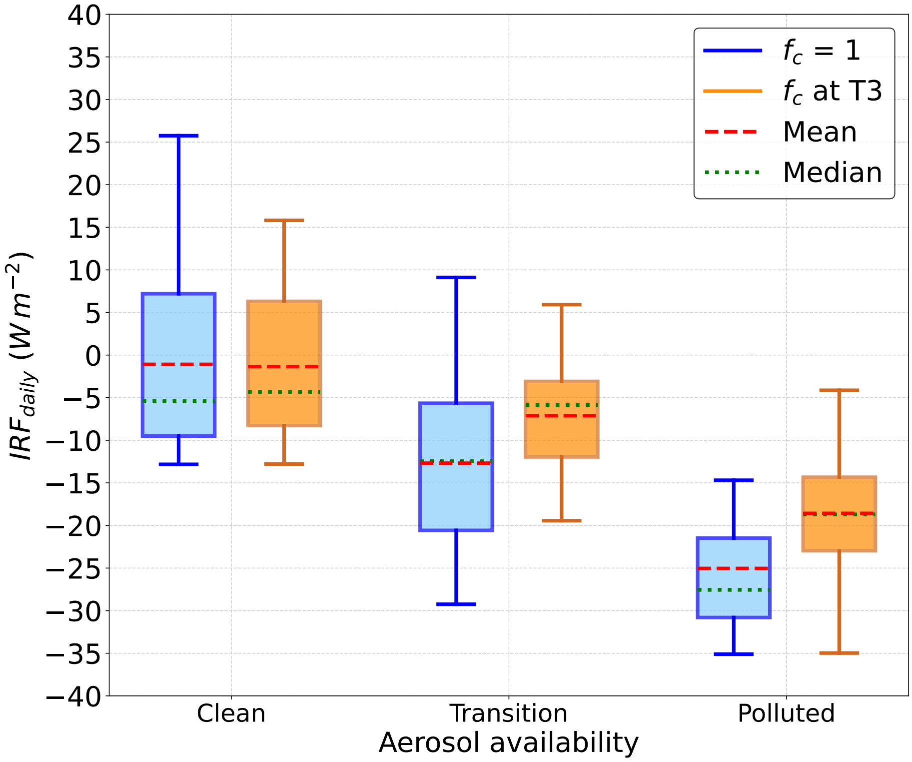

Figure 7. Boxplots, means and medians of IRF$_{daily}$ calculated according to the first clean atmosphere reference for 2015 and separated according to the aerosol availability at T3.

The boxplots discussed above were complemented by histograms of the annual IRF$_{daily}$ distributions for 2014 and 2015, shown in Figs. 8 and 9. The results in Fig. 8 indicate that the overall statistics for 2014 are more negative than those for 2015: the 2015 median corresponds to about 47% of that for 2014, whereas the mean represents 66% of the 2014 mean. The results scaled by the daytime mean f$_c$ (Fig. 9) display more homogeneous distributions approaching normality, with the lower and upper quartiles of the corresponding boxplots confined to narrower intervals than those for the distributions that ignore f$_c$ variability at T3. This outcome suggests that multiplying by the daytime mean f$_c$ effectively selects and constrains the final dataset, removing extreme values and producing probability density functions with reduced kurtosis magnitude.

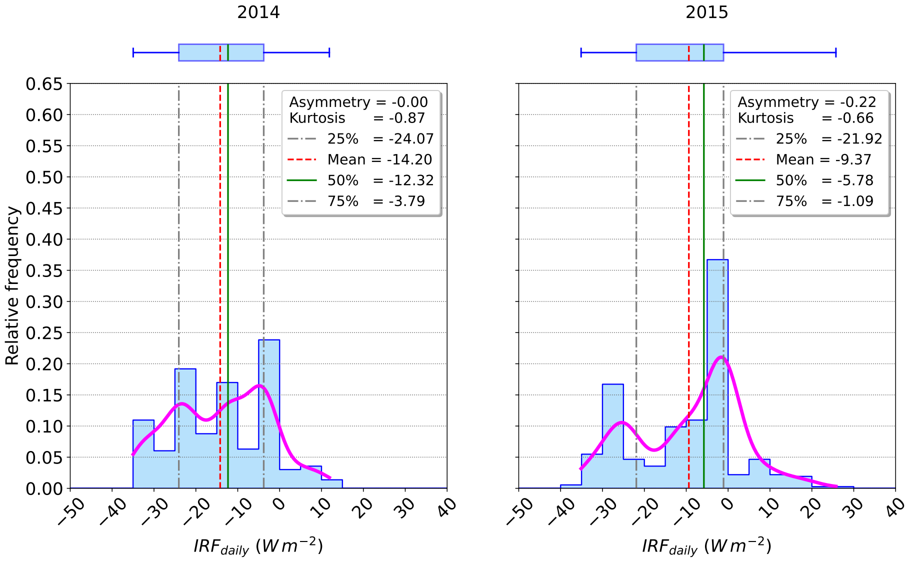

Figure 8. Boxplots and histograms of IRF_{daily} for 2014 (left) and 2015 (right) for $f_c = 1$.

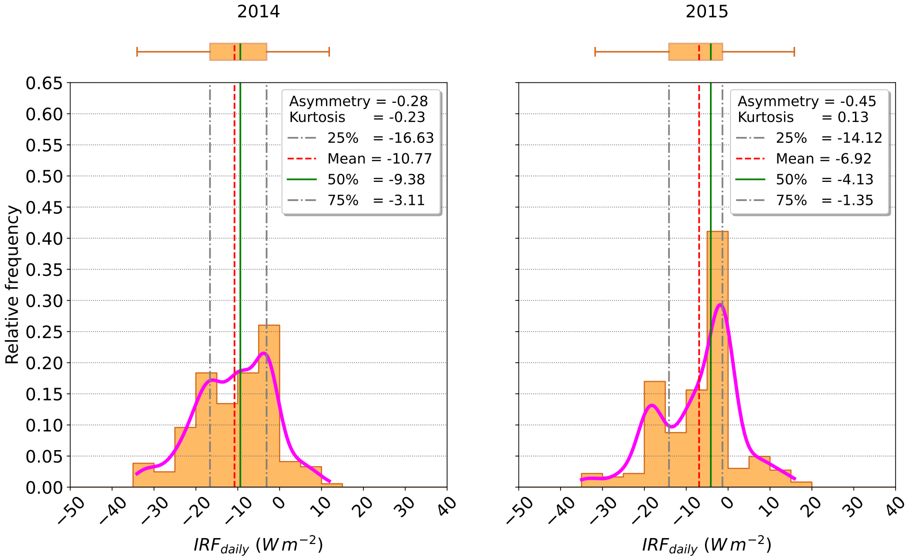

Figure 9. Boxplots and histograms of IRF_{daily} for 2014 and 2015 for f_c observed in the T3 site.

3.2 Second clean state - “Sazonal” irradiance reference

The IRF_{daily} values obtained using a variable irradiance value for a clean-atmosphere reference are presented here. It is important to recall that this seasonal irradiance reference approach aimed to reduce the likelihood that the results would be

https://doi.org/10.5194/egusphere-2026-996
Preprint. Discussion started: 7 April 2026

influenced by the natural atmospheric variability over T3, thereby better isolating the aerosol effect on warm clouds. As shown in Fig. 10, the IRF$_{daily}$ values in this case fluctuate around zero, unlike the forcings computed using the fixed irradiance reference value (Fig. 5). Nevertheless, the results are, on average, nearly constant throughout 2014 and 2015, with most data points exhibiting negative values. Subtle variations can also be observed that may or may not be associated, on average, with 340 aerosol properties.

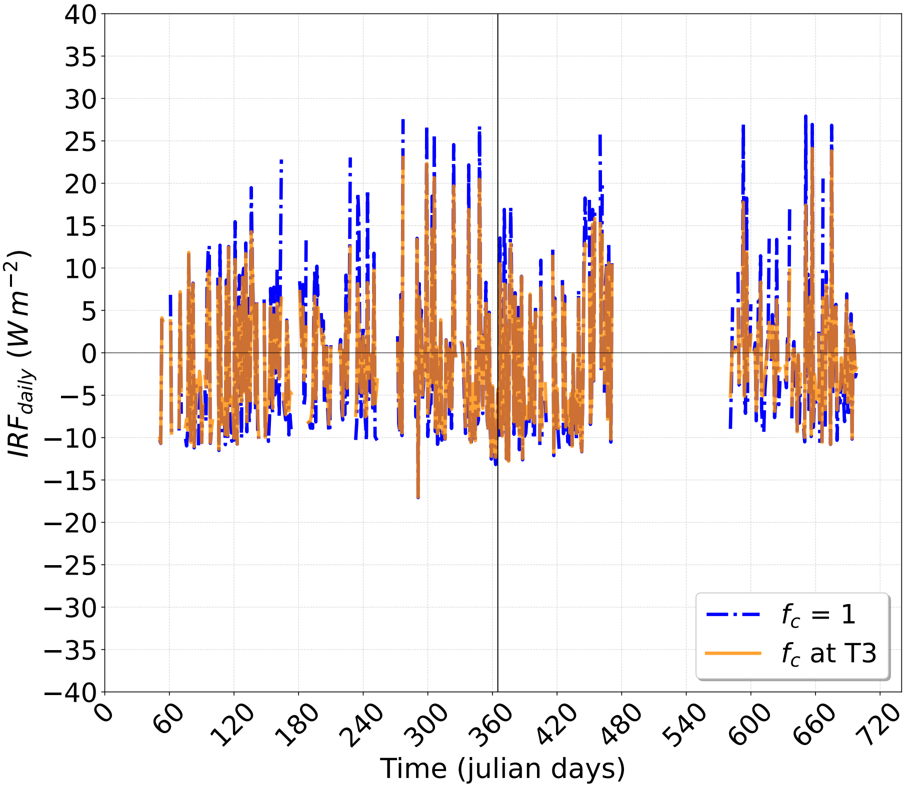

Figure 10. IRF$_{daily}$ calculated according to the variable reference for clean atmosphere for 2014 and 2015. The blue line shows the results for an f$_c$ of 100%, while the gold line shows the values according to the f$_c$ measured in T3. Vertical scale as in Fig. 5 for comparison.

The IRF$_{daily}$ boxplots for the different aerosol-loading scenarios in 2014 and 2015 (Figs. 11 and 12, respectively) indicate that the distributions multiplied by the measured f$_c$ at T3 are more homogeneous and less skewed than those that do not account for this parameter. The distributions for all scenarios in both years show central values (between the twenty-fifth and seventy-fifth percentiles) between -10 $\mathrm{W\,m^{-2}}$ and approximately +8.0 $\mathrm{W\,m^{-2}}$. The means and medians for the clean and polluted 345 scenarios of the two years are negative, with greater magnitudes for the clean periods. This behavior, associated with a larger dispersion of IRF$_{daily}$ values during cleaner conditions, can be explained—at least for the distributions that do not include the T3's cloud fraction—by greater variability in the r$_{eff.}$ values of the modeled clouds in clean periods. For the results multiplied by f_c, this effect may also occur, as higher f_c values during clean conditions make the means and medians even more negative than those observed during polluted periods.

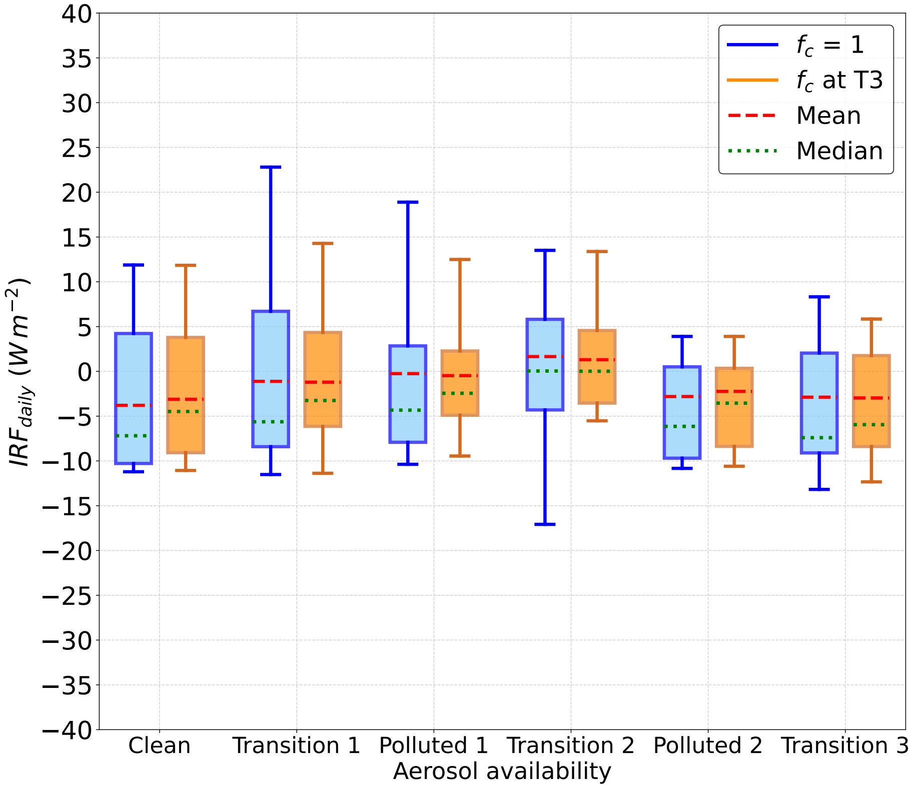

Figure 11. Boxplots, means and medians of IRF_{daily} calculated for the second clean atmosphere reference for 2014 and separated according to the different aerosol availability at T3.

The results derived from the variable irradiance reference allow the derivation of annual statistics in which the first indirect aerosol effect is more clearly isolated. The resulting statistics for 2014 and 2015 (Figs. 13 and 14) show that, compared to the values obtained using the fixed irradiance reference, the IRF_{daily} magnitudes are smaller. The effect of seasonal variations in atmospheric conditions on the warm-cloud droplet size is illustrated by the percentage variations in the mean $r_{eff.}$ during the clean periods of 2014 and 2015 relative to the mean $r_{eff.}$ of the clean reference state. These differences were 21.6% and 20.7%, respectively, while the polluted periods exhibited reductions of 18.7% for both years. The percentage variations in TOA flux were 1.62% and 0.50% for the clean intervals, while for the polluted intervals, there were increases of 0.82% and 0.34%, even though LWC was assumed to be the same for both clean and polluted periods.

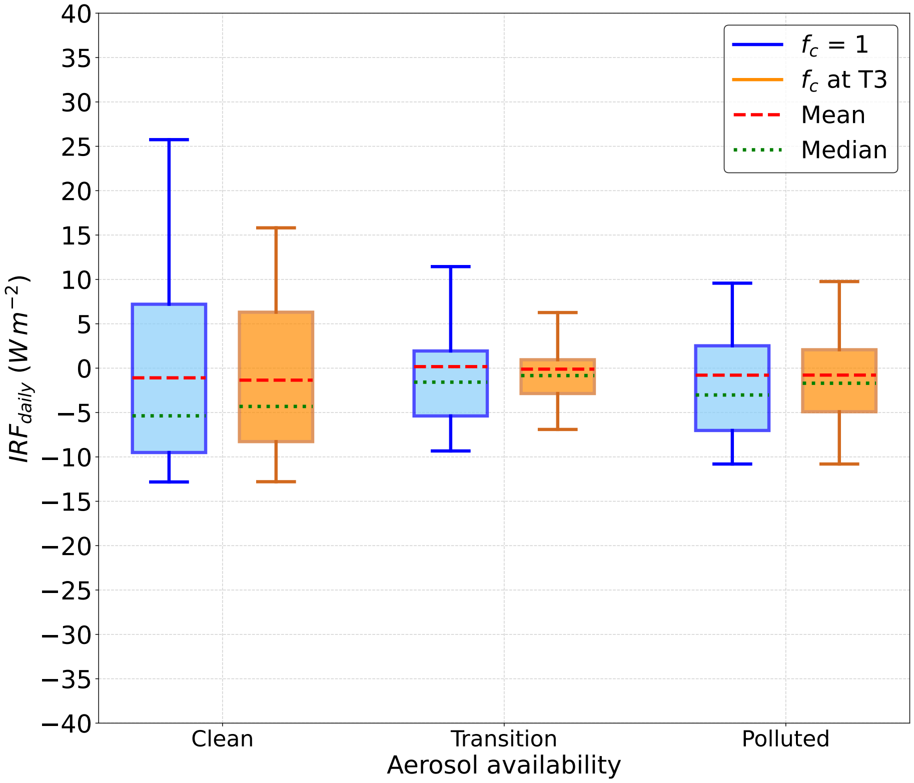

Figure 12. Statistics of IRF$_{daily}$ calculated for the second clean atmosphere reference for 2015 and separated according to the different aerosol availability at T3.

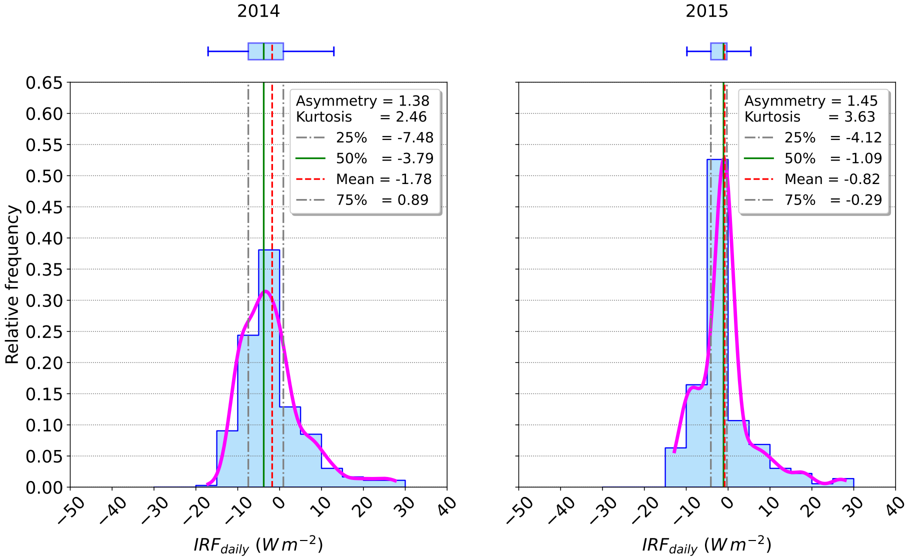

Figure 13. Boxplots and histograms of IRF$_{daily}$ for 2014 and 2015 for f$_c$ = 1 according to the second reference for a clean atmosphere.

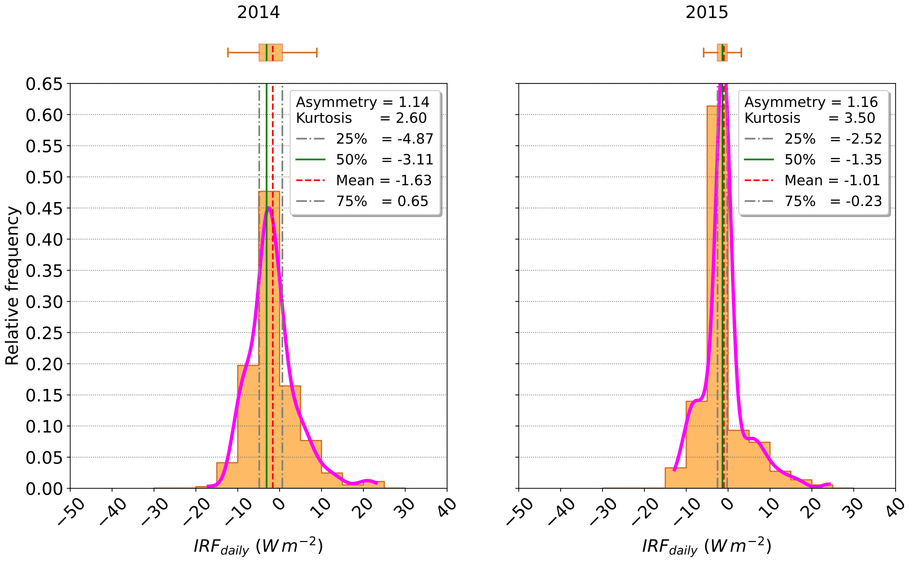

Figure 14. Boxplots and histograms of IRF$_{daily}$ for 2014 and 2015 for f$_c$ = 1 measured at T3, according to the second reference for a clean atmosphere.

3.3 IRFaci sensibilities for clean and polluted scenarios

According to Wei et al. (2020), aerosol optical depth (AOD) is widely recognized as a critical indicator to understand atmospheric physics and regional air quality due to its ability to quantify aerosol loading in the atmosphere. Considering this, one way to assess the sensitivity of daily instantaneous forcings to aerosol availability during the clean period of a given year is to compute the ratio between the mean IRF$_{daily}$ for the clean season and the percentage variation of AOD for the same clean period. The same procedure can then be applied to the polluted season of that year, and the sensitivities obtained for the clean and polluted periods can be compared.

Table 5 presents the calculated sensitivities for the clean and polluted periods of 2014 and 2015, derived from the results based on the seasonal irradiance reference while assuming f$_c$ = 1. The results indicate that the sensitivity of low warm clouds to variations in aerosol load may be greater under cleaner atmospheric conditions than in already highly polluted environments.

4 Summary and Discusion

The instantaneous radiative forcings due to the first indirect aerosol effect obtained in this study were separated into those calculated using a constant irradiance reference and those derived from a seasonal irradiance reference. The annual means for f$_c$ = 1 in 2014 and 2015, corresponding to the fixed reference, were -14.20 [-24.07; -3.79] $\mathrm{W\,m^{-2}}$ and -9.37 [-21.92; -1.09] $\mathrm{W\,m^{-2}}$, respectively. For the seasonal reference, the results were -1.78 [-7.48; 0.89] $\mathrm{W\,m^{-2}}$ and -0.82 [-4.12; -0.29] $\mathrm{W\,m^{-2}}$, while the interquartile ranges (IQR) were 8.37 $\mathrm{W\,m^{-2}}$ and 3.83 $\mathrm{W\,m^{-2}}$, significantly smaller than those obtained for the fixed-irradiance reference (20.28 and 20.83 $\mathrm{W\,m^{-2}}$). These results demonstrate greater IRFaci variability in 2014 than in 2015 and indicate a

https://doi.org/10.5194/egusphere-2026-996
Preprint. Discussion started: 7 April 2026

Table 5. Percentage variations of AOD ("ΔAOD") and daily IRFaci sensitivities according to the clean and the polluted periods of 2014 and 2015. The average AOD values for the constituent days of the clean and the polluted references were equal to 0.07 and 0.20, respectively. The average IRF$_{daily}$ for the polluted period of 2014, equal to -1.53 $\mathrm{W\,m^{-2}}$, was calculated from the values referring to the two polluted sub-periods of 2014 (-0.25 and -2.81 $\mathrm{W\,m^{-2}}$, respectively).

Year - Scenario	$\lvert$Mean IRF$_{\mathrm{daily}}\rvert$ ($\mathrm{W\,m^{-2}}$)	Mean AOD	ΔAOD (%)	Sensibility x 100 ($\mathrm{W\,m^{-2}}/\Delta$AOD)
2014 - Clean	3.79	0.09	31.26	12.12
2014 - Polluted	1.53	0.28	37.54	4.08
2015 - Clean	1.09	0.13	81.10	1.34
2015 - Polluted	0.79	0.59	191.04	0.41

reduced degree of uncertainty when accounting for seasonal variations in the microphysical structure of the analyzed clouds. Given that CCN and AOD concentrations were notably high during the second half of both years, these results are consistent in magnitude with previous findings (e.g. Wall et al., 2023; Wang et al., 2023).

For both references, positive IRF$_{daily}$ values were obtained. These correspond to instances in which the reference TOA upward irradiance exceeded that of the perturbed state. This does not imply that low warm clouds have a net warming effect on the surface. As the warm-cloud models were constructed from daily statistical distributions of CBH, CTH, LWC, and r$_{eff.}$, the occurrence of positive instantaneous forcings arises from the adopted methodology itself, which sought to reflect the natural variability of daytime cloud properties. Furthermore, it should be noted that the days selected to represent the two reference states were chosen based on aerosol availability rather than warm-cloud characteristics. Therefore, daily fluctuations in irradiances and IRF$_{daily}$ values are expected, representing the natural day-to-day variability of low warm-cloud properties.

For both references, interannual differences were observed, with more intense IRF values occurring in 2014. Since the first reference, obtained using a simpler and more direct procedure, assumes a fixed irradiance value for the entire GoAmazon2014/5 period, larger IRF magnitudes are expected—particularly during polluted periods. This first reference involves fewer intermediate assumptions than the second and does not require non-contaminated data from polluted seasons. However, it neglects the seasonal variability of the atmosphere's natural conditions over the study period, which may influence the microphysics of the analyzed clouds and the resulting IRF. The variable irradiance reference, in turn, follows the seasonal atmospheric variations, reducing the likelihood that the results are biased by natural variability. Thus, although it represents a first-order approximation, the results obtained using the seasonal irradiance reference are more appropriate for analyzing instantaneous radiative forcings associated with the first indirect aerosol effect.

The differences between IRFaci values computed using the two reference states align with Gryspeerdt et al. (2023), who emphasized the importance of clean-atmosphere states in determining resultant instantaneous forcings. The slightly higher percentage variations in integrated TOA flux during clean periods compared to polluted ones highlight the influence of cleaner atmospheric conditions on IRFaci calculations. The results in Table 5 further indicate that low warm clouds may exhibit greater sensitivity to anthropogenic aerosols under cleaner conditions than in atmospheres already affected by high pollution levels.

The daily IRFaci values obtained when considering f_c variations at T3 and using the seasonal irradiance reference were -1.63 [-4.87; 0.65] $\mathrm{W\,m^{-2}}$ and -1.01 [-2.52; -0.23] $\mathrm{W\,m^{-2}}$ for 2014 and 2015, respectively. The IRFaci values associated with the first indirect effect during the GoAmazon2014/5 campaign (averaged from the IRF_{daily} means of 2014 and 2015, for f_c = 1) corresponding to the two reference approaches were -11.79 [-23.0; -2.44] $\mathrm{W\,m^{-2}}$ and -1.30 [-5.8; 0.59] $\mathrm{W\,m^{-2}}$, respectively. Despite differing observational conditions (experimental platform and reference irradiance), both sets of results fall within the range reported by Herbert and Stier (2023), namely total instantaneous forcings—largely due to biomass-burning aerosols—of up to -50 $\mathrm{W\,m^{-2}}$ for AOD $\approx$ 1.

Although direct comparison must be interpreted with caution, the second clean-atmosphere reference yielded IRFaci values closer to the estimate (-0.7 ± 0.5 $\mathrm{W\,m^{-2}}$, specifically related to the Twomey effect) reported in the latest IPCC Assessment (Forster et al., 2021). This underscores the importance of defining an appropriate atmospheric reference state in IRFaci calculations, which are significantly influenced by the chosen irradiance baseline.

5 Conclusions

Quantification of IRFaci associated with warm clouds in the Amazon was achieved by evaluating the first indirect aerosol effect in the region, using an unique approach that combines in situ measurements, ground-based observations, and cloud modeling based on these datasets.

The IRFaci values calculated using the fixed irradiance reference became increasingly negative as polluted scenarios approached. The averages computed for f_c = 100% and for f_c measured at T3 are virtually identical under clean atmospheric conditions, which is not the case for polluted scenarios. This indicates that, although cloud cover is greater during cleaner periods, the influence of cloud cover on the amount of radiation reflected to space becomes more significant under polluted conditions.

Using of the seasonal irradiance reference reduced the variance of the resulting IRFaci, which oscillated around zero—unlike the forcings derived from the fixed irradiance reference. In addition, the IRFaci values obtained with the seasonal reference exhibited distributions with higher positive skewness, predominated by values smaller than the negative mean. The resulting interquartile range was also smaller, indicating reduced uncertainties.

The result obtained for GoAmazon2014/5 (-11.8 $\mathrm{W\,m^{-2}}$ when f_c = 1 for the first clean-atmosphere reference) presents an order of magnitude consistent with previous studies. The value obtained using the second reference (-1.3 $\mathrm{W\,m^{-2}}$) is closer to the latest estimate reported by the IPCC. The percentage variations of AOD and IRFaci sensitivities for the clean and polluted periods of 2014 (31.3% and 37.5%; 12.1 and 4.1 $\mathrm{W\,m^{-2}}$ per %) and 2015 (81.1% and 191.0%; 1.3 and 0.4 $\mathrm{W\,m^{-2}}$ per %) suggest that the sensitivity of low warm clouds to anthropogenic aerosols may be greater under clean conditions than in atmospheres already affected by high pollution levels.

The results obtained stem from an effort to estimate instantaneous radiative forcings entirely from in situ and ground-based remote sensing data collected over the Amazon. This represents a unique approach to calculating instantaneous radiative forcings associated with the first indirect effect of anthropogenic aerosols on warm clouds in the region. The findings contribute to a better understanding of the first indirect effect related to the influence that anthropogenic aerosols may exert on low warm clouds in the Amazon and can also serve as a reference for model evaluation and future studies aiming to quantify IRFaci or ERFaci in the region.

Data availability. Publicly available datasets were analyzed in this study. These data can be found at ARM: https://adc.arm.gov/discovery/, accessed on 20 February 2026 19:50 UTC, and HALO database: https://halo-db.pa.op.dlr.de/mission/5, accessed on 20 February 2026 19:50 UTC.

Author contributions. Pugliesi, A. C. and Correia, A. L. conceptualized the study. Pugliesi, A. C. and Cecchini, M. curated the data. Pugliesi, A. C. initiated the study, developed the methodology, performed the simulations and did the investigation and formal analysis. Pugliesi, A. C. prepared the manuscript. Correia, A. L. and Cecchini, M. review the manuscript. All authors have read and agreed to the published version of the manuscript.

Competing interests. The authors declare that they have no conflict of interest.

Acknowledgements. We thank ARM, G-1 and HALO teams for the datasets used in this study. We also thank everyone involved in organizing and carrying out the GoAmazon2014/5 campaign. Andre Cezar Pugliesi thanks the Coordination for the Improvement of Higher Education Personnel (*Coordenação de Aperfeiçoamento de Pessoal de Nível Superior*, CAPES, Brazil) and the *São Paulo* Research Foundation (FAPESP, Brazil) for research grants 88882.332852/2010-01 and 2024/17448-9, respectively. Micael A. Cecchini was funded by FAPESP grant 2022/13257-9, *Serrapilheira* grant 2211-41823. Andre Cezar Pugliesi acknowledges the use of Grammarly (https://www.grammarly.com/) to improve the grammar of this manuscript. After using this tool, the authors reviewed and revised the text as needed and assume full responsibility for the content of the manuscript.

References

Albrecht, B. A.: Aerosols, Cloud Microphysics, and Fractional Cloudiness, Science, 245, 1227–1230, https://doi.org/10.1126/science.245.4923.1227, 1989.

Alexandrov, M. D., Marshak, A., Cairns, B., Lacis, A. A., and Carlson, B. E.: Automated Cloud Screening Algorithm for MFRSR Data, Geophysical Research Letters, 31, https://doi.org/10.1029/2003GL019105, 2004.

Carslaw, K. S., Lee, L. A., Reddington, C. L., Pringle, K. J., Rap, A., Forster, P. M., Mann, G. W., Spracklen, D. V., Woodhouse, M. T., Regayre, L. A., and Pierce, J. R.: Large Contribution of Natural Aerosols to Uncertainty in Indirect Forcing, Nature, 503, 67–71, https://doi.org/10.1038/nature12674, 2013.

Cecchini, M. A., Machado, L. A. T., Comstock, J. M., Mei, F., Wang, J., Fan, J., Tomlinson, J. M., Schmid, B., Albrecht, R., Martin, S. T., and Artaxo, P.: Impacts of the Manaus Pollution Plume on the Microphysical Properties of Amazonian Warm-Phase Clouds in the Wet Season, Atmospheric Chemistry and Physics, 16, 7029–7041, https://doi.org/10.5194/acp-16-7029-2016, 2016.

Chen, Y.-C., Christensen, M. W., Stephens, G. L., and Seinfeld, J. H.: Satellite-Based Estimate of Global Aerosol–Cloud Radiative Forcing by Marine Warm Clouds, Nature Geoscience, 7, 643–646, https://doi.org/10.1038/ngeo2214, 2014.

Christensen, M. W., Neubauer, D., Poulsen, C. A., Thomas, G. E., McGarragh, G. R., Povey, A. C., Proud, S. R., and Grainger, R. G.: Unveiling Aerosol–Cloud Interactions – Part 1: Cloud Contamination in Satellite Products Enhances the Aerosol Indirect Forcing Estimate, Atmospheric Chemistry and Physics, 17, 13 151–13 164, https://doi.org/10.5194/acp-17-13151-2017, 2017.

Diamond, M. S., Director, H. M., Eastman, R., Possner, A., and Wood, R.: Substantial Cloud Brightening From Shipping in Subtropical Low Clouds, AGU Advances, 1, e2019AV000 111, https://doi.org/10.1029/2019AV000111, 2020.

Dong, X. and Mace, G. G.: Arctic Stratus Cloud Properties and Radiative Forcing Derived from Ground-Based Data Collected at Barrow, Alaska, Journal of Climate, 16, 445–461, https://doi.org/10.1175/1520-0442(2003)016<0445:ASCPAR>2.0.CO;2, 2003.

Dürr, B. and Philipona, R.: Automatic Cloud Amount Detection by Surface Longwave Downward Radiation Measurements, Journal of Geophysical Research: Atmospheres, 109, https://doi.org/10.1029/2003JD004182, 2004.

Emde, C., Buras-Schnell, R., Kylling, A., Mayer, B., Gasteiger, J., Hamann, U., Kylling, J., Richter, B., Pause, C., Dowling, T., and Bugliaro, L.: The libRadtran Software Package for Radiative Transfer Calculations (Version 2.0.1), Geoscientific Model Development, 9, 1647–1672, https://doi.org/10.5194/gmd-9-1647-2016, 2016.

Forster, P., Storelvmo, T., Armour, K., Collins, W., Dufresne, J. L., Frame, D., Lunt, D. J., Mauritsen, T., Palmer, M. D., Watanabe, M., Wild, M., and Zhang, H.: The Earth's Energy Budget, Climate Feedbacks and Climate Sensitivity, Tech. rep., Cambridge University Press, https://doi.org/10.1017/9781009157896.009, 2021.

Gasteiger, J., Emde, C., Mayer, B., Buras, R., Buehler, S. A., and Lemke, O.: Representative Wavelengths Absorption Parameterization Applied to Satellite Channels and Spectral Bands, Journal of Quantitative Spectroscopy and Radiative Transfer, 148, 99–115, https://doi.org/10.1016/j.jqsrt.2014.06.024, 2014.

Giles, D. M., Sinyuk, A., Sorokin, M. G., Schafer, J. S., Smirnov, A., Slutsker, I., Eck, T. F., Holben, B. N., Lewis, J. R., Campbell, J. R., Welton, E. J., Korkin, S. V., and Lyapustin, A. I.: Advancements in the Aerosol Robotic Network (AERONET) Version 3 Database – Automated near-Real-Time Quality Control Algorithm with Improved Cloud Screening for Sun Photometer Aerosol Optical Depth (AOD) Measurements, Atmospheric Measurement Techniques, 12, 169–209, https://doi.org/10.5194/amt-12-169-2019, 2019.

Gryspeerdt, E., Povey, A. C., Grainger, R. G., Hasekamp, O., Hsu, N. C., Mulcahy, J. P., Sayer, A. M., and Sorooshian, A.: Uncertainty in Aerosol–Cloud Radiative Forcing Is Driven by Clean Conditions, Atmospheric Chemistry and Physics, 23, 4115–4122, https://doi.org/10.5194/acp-23-4115-2023, 2023.

Hamilton, D. S., Lee, L. A., Pringle, K. J., Reddington, C. L., Spracklen, D. V., and Carslaw, K. S.: Occurrence of Pristine Aerosol Environments on a Polluted Planet, Proceedings of the National Academy of Sciences, 111, 18 466–18 471, https://doi.org/10.1073/pnas.1415440111, 2014.

Harrison, L. and Michalsky, J.: Objective Algorithms for the Retrieval of Optical Depths from Ground-Based Measurements, Applied Optics, 33, 5126–5132, https://doi.org/10.1364/AO.33.005126, 1994.

Hasekamp, O. P., Gryspeerdt, E., and Quaas, J.: Analysis of Polarimetric Satellite Measurements Suggests Stronger Cooling Due to Aerosol-Cloud Interactions, Nature Communications, 10, 5405, https://doi.org/10.1038/s41467-019-13372-2, 2019.

Haywood, J. and Boucher, O.: Estimates of the Direct and Indirect Radiative Forcing Due to Tropospheric Aerosols: A Review, Reviews of Geophysics, 38, 513–543, https://doi.org/10.1029/1999RG000078, 2000.

Herbert, R. and Stier, P.: Satellite Observations of Smoke–Cloud–Radiation Interactions over the Amazon Rainforest, Atmospheric Chemistry and Physics, 23, 4595–4616, https://doi.org/10.5194/acp-23-4595-2023, 2023.

Hess, M., Koepke, P., and Schult, I.: Optical Properties of Aerosols and Clouds: The Software Package OPAC, Bulletin of the American Meteorological Society, https://journals.ametsoc.org/view/journals/bams/79/5/1520-0477_1998_079_0831_opoaac_2_0_co_2.xml, 1998.

Heyn, I., Block, K., Mülmenstädt, J., Gryspeerdt, E., Kühne, P., Salzmann, M., and Quaas, J.: Assessment of Simulated Aerosol Effective Radiative Forcings in the Terrestrial Spectrum, Geophysical Research Letters, 44, 1001–1007, https://doi.org/10.1002/2016GL071975, 2017.

IPCC: Climate Change 2013: The Physical Science Basis. Contribution of Working Group I to the Fifth Assessment Report of the Intergovernmental Panel on Climate Change [Stocker, T.F., D. Qin, G.-K. Plattner, M. Tignor, S.K. Allen, J. Boschung, A. Nauels, Y. Xia, V. Bex and P.M. Midgley (Eds.)]. Cambridge University Press, Cambridge, United Kingdom and New York, NY, USA, 1535 Pp., Cambridge University Press, 2013.

Keeling, R. F., Morgan, E. J., and Keeling, C. D.: Atmospheric Monthly In Situ CO2 Data - Mauna Loa Observatory, Hawaii (Archive 2024-11-13). In Scripps CO2 Program Data. UC San Diego Library Digital Collections., https://doi.org/10.6075/J08W3BHW, 2017.

Keil, A. and Haywood, J. M.: Solar Radiative Forcing by Biomass Burning Aerosol Particles during SAFARI 2000: A Case Study Based on Measured Aerosol and Cloud Properties, Journal of Geophysical Research: Atmospheres, 108, https://doi.org/10.1029/2002JD002315, 2003.

King, W. D., Parkin, D. A., and Handsworth, R. J.: A Hot-Wire Liquid Water Device Having Fully Calculable Response Characteristics, Journal of Applied Meteorology and Climatology, 17, 1809–1813, https://doi.org/10.1175/1520-0450(1978)017<1809:AHWLWD>2.0.CO;2, 1978.

Kollias, P., Miller, M. A., Luke, E. P., Johnson, K. L., Clothiaux, E. E., Moran, K. P., Widener, K. B., and Albrecht, B. A.: The Atmospheric Radiation Measurement Program Cloud Profiling Radars: Second-Generation Sampling Strategies, Processing, and Cloud Data Products, Journal of Atmospheric and Oceanic Technology, 24, 1199–1214, https://doi.org/10.1175/JTECH2033.1, 2007.

Lebsock, M. D., Stephens, G. L., and Kummerow, C.: Multisensor Satellite Observations of Aerosol Effects on Warm Clouds, Journal of Geophysical Research: Atmospheres, 113, https://doi.org/10.1029/2008JD009876, 2008.

Lee, L. A., Reddington, C. L., and Carslaw, K. S.: On the Relationship between Aerosol Model Uncertainty and Radiative Forcing Uncertainty, Proceedings of the National Academy of Sciences, 113, 5820–5827, https://doi.org/10.1073/pnas.1507050113, 2016.

Levitus, S., Antonov, J. I., Boyer, T. P., Baranova, O. K., Garcia, H. E., Locarnini, R. A., Mishonov, A. V., Reagan, J. R., Seidov, D., Yarosh, E. S., and Zweng, M. M.: World Ocean Heat Content and Thermosteric Sea Level Change (0–2000 m), 1955–2010, Geophysical Research Letters, 39, https://doi.org/10.1029/2012GL051106, 2012.

Lloyd, S.: Least Squares Quantization in PCM, IEEE Transactions on Information Theory, 28, 129–137, https://doi.org/10.1109/TIT.1982.1056489, 1982.

Long, C. N., Ackerman, T. P., Gaustad, K. L., and Cole, J. N. S.: Estimation of Fractional Sky Cover from Broadband Shortwave Radiometer Measurements, Journal of Geophysical Research: Atmospheres, 111, https://doi.org/10.1029/2005JD006475, 2006.

Mace, G. G., Benson, S., and Kato, S.: Cloud Radiative Forcing at the Atmospheric Radiation Measurement Program Climate Research Facility: 2. Vertical Redistribution of Radiant Energy by Clouds, Journal of Geophysical Research: Atmospheres, 111, https://doi.org/10.1029/2005JD005922, 2006.

Machado, L. A. T., Calheiros, A. J. P., Biscaro, T., Giangrande, S., Silva Dias, M. A. F., Cecchini, M. A., Albrecht, R., Andreae, M. O., Araujo, W. F., Artaxo, P., Borrmann, S., Braga, R., Burleyson, C., Eichholz, C. W., Fan, J., Feng, Z., Fisch, G. F., Jensen, M. P., Martin, S. T., Pöschl, U., Pöhlker, C., Pöhlker, M. L., Ribaud, J.-F., Rosenfeld, D., Saraiva, J. M. B., Schumacher, C., Thalman, R., Walter, D., and Wendisch, M.: Overview: Precipitation Characteristics and Sensitivities to Environmental Conditions during GoAmazon2014/5 and ACRIDICON-CHUVA, Atmospheric Chemistry and Physics, 18, 6461–6482, https://doi.org/10.5194/acp-18-6461-2018, 2018.

Marsing, A., Meerkötter, R., Heller, R., Kaufmann, S., Jurkat-Witschas, T., Krämer, M., Rolf, C., and Voigt, C.: Investigating the Radiative Effect of Arctic Cirrus Measured in Situ during the Winter 2015–2016, Atmospheric Chemistry and Physics, 23, 587–609, https://doi.org/10.5194/acp-23-587-2023, 2023.

Martin, S. T., Artaxo, P., Machado, L. a. T., Manzi, A. O., Souza, R. a. F., Schumacher, C., Wang, J., Andreae, M. O., Barbosa, H. M. J., Fan, J., Fisch, G., Goldstein, A. H., Guenther, A., Jimenez, J. L., Pöschl, U., Silva Dias, M. A., Smith, J. N., and Wendisch, M.: Introduction: Observations and Modeling of the Green Ocean Amazon (GoAmazon2014/5), Atmospheric Chemistry and Physics, 16, 4785–4797, https://doi.org/10.5194/acp-16-4785-2016, 2016.

Martins, J. V., Marshak, A., Remer, L. A., Rosenfeld, D., Kaufman, Y. J., Fernandez-Borda, R., Koren, I., Correia, A. L., Zubko, V., and Artaxo, P.: Remote Sensing the Vertical Profile of Cloud Droplet Effective Radius, Thermodynamic Phase, and Temperature, Atmospheric Chemistry and Physics, 11, 9485–9501, https://doi.org/10.5194/acp-11-9485-2011, 2011.

Michalsky, J. J., Schlemmer, J. A., Berkheiser, W. E., Berndt, J. L., Harrison, L. C., Laulainen, N. S., Larson, N. R., and Barnard, J. C.: Multiyear Measurements of Aerosol Optical Depth in the Atmospheric Radiation Measurement and Quantitative Links Programs, Journal of Geophysical Research: Atmospheres, 106, 12 099–12 107, https://doi.org/10.1029/2001JD900096, 2001.

Mie, G.: Beiträge Zur Optik Trüber Medien, Speziell Kolloidaler Metallösungen, Annalen der Physik, 330, 377–445, https://doi.org/10.1002/andp.19083300302, 1908.

Morrison, H., Curry, J. A., and Khvorostyanov, V. I.: A New Double-Moment Microphysics Parameterization for Application in Cloud and Climate Models. Part I: Description, Journal of the Atmospheric Sciences, 62, 1665–1677, https://doi.org/10.1175/JAS3446.1, 2005.

Mülmenstädt, J. and Feingold, G.: The Radiative Forcing of Aerosol–Cloud Interactions in Liquid Clouds: Wrestling and Embracing Uncertainty, Current Climate Change Reports, 4, 23–40, https://doi.org/10.1007/s40641-018-0089-y, 2018.

Petters, M. D. and Kreidenweis, S. M.: A Single Parameter Representation of Hygroscopic Growth and Cloud Condensation Nucleus Activity, Atmospheric Chemistry and Physics, 7, 1961–1971, https://doi.org/10.5194/acp-7-1961-2007, 2007.

Pöschl, U., Martin, S. T., Sinha, B., Chen, Q., Gunthe, S. S., Huffman, J. A., Borrmann, S., Farmer, D. K., Garland, R. M., Helas, G., Jimenez, J. L., King, S. M., Manzi, A., Mikhailov, E., Pauliquevis, T., Petters, M. D., Prenni, A. J., Roldin, P., Rose, D., Schneider, J., Su, H., Zorn,

S. R., Artaxo, P., and Andreae, M. O.: Rainforest Aerosols as Biogenic Nuclei of Clouds and Precipitation in the Amazon, Science, 329, 1513–1516, https://doi.org/10.1126/science.1191056, 2010.

Quaas, J., Ming, Y., Menon, S., Takemura, T., Wang, M., Penner, J. E., Gettelman, A., Lohmann, U., Bellouin, N., Boucher, O., Sayer, A. M., Thomas, G. E., McComiskey, A., Feingold, G., Hoose, C., Kristjánsson, J. E., Liu, X., Balkanski, Y., Donner, L. J., Ginoux, P. A., Stier, P., Grandey, B., Feichter, J., Sednev, I., Bauer, S. E., Koch, D., Grainger, R. G., Kirkev&aring, G, A., Iversen, T., Seland, Ø., Easter, R., Ghan, S. J., Rasch, P. J., Morrison, H., Lamarque, J.-F., Iacono, M. J., Kinne, S., and Schulz, M.: Aerosol Indirect Effects – General Circulation Model Intercomparison and Evaluation with Satellite Data, Atmospheric Chemistry and Physics, 9, 8697–8717, https://doi.org/10.5194/acp-9-8697-2009, 2009.

Reid, J. S., Hobbs, P. V., Rangno, A. L., and Hegg, D. A.: Relationships between Cloud Droplet Effective Radius, Liquid Water Content, and Droplet Concentration for Warm Clouds in Brazil Embedded in Biomass Smoke, Journal of Geophysical Research: Atmospheres, 104, 6145–6153, https://doi.org/10.1029/1998JD200119, 1999.

Riihimaki, L., Gaustad, K., and Long, C.: Radiative Flux Analysis (RADFLUXANAL) Value-Added Product: Retrieval of Clear-Sky Broadband Radiative Fluxes and Other Derived Values, Tech. Rep. DOE/SC-ARM-TR–228, 1569477, DOE-ARM, https://doi.org/10.2172/1569477, 2019.

Rosenfeld, D. and Woodley, W. L.: Closing the 50-Year Circle: From Cloud Seeding to Space and Back to Climate Change through Precipitation Physics, in: Cloud Systems, Hurricanes, and the Tropical Rainfall Measuring Mission (TRMM), pp. 59–80, Meteorological Monographs, American Meteorological Society, 2003.

Santer, B. D., Painter, J. F., Bonfils, C., Mears, C. A., Solomon, S., Wigley, T. M. L., Gleckler, P. J., Schmidt, G. A., Doutriaux, C., Gillett, N. P., Taylor, K. E., Thorne, P. W., and Wentz, F. J.: Human and Natural Influences on the Changing Thermal Structure of the Atmosphere, Proceedings of the National Academy of Sciences, 110, 17 235–17 240, https://doi.org/10.1073/pnas.1305332110, 2013.

Schmid, B., Tomlinson, J. M., Hubbe, J. M., Comstock, J. M., Mei, F., Chand, D., Pekour, M. S., Kluzek, C. D., Andrews, E., Biraud, S. C., and McFarquhar, G. M.: The DOE ARM Aerial Facility, Bulletin of the American Meteorological Society, 95, 723–742, https://doi.org/10.1175/BAMS-D-13-00040.1, 2014.

Solomon, S., Rosenlof, K. H., Portmann, R. W., Daniel, J. S., Davis, S. M., Sanford, T. J., and Plattner, G.-K.: Contributions of Stratospheric Water Vapor to Decadal Changes in the Rate of Global Warming, Science, 327, 1219–1223, https://doi.org/10.1126/science.1182488, 2010.

Stamnes, K., Tsay, S.-C., Wiscombe, W., and Jayaweera, K.: Numerically Stable Algorithm for Discrete-Ordinate-Method Radiative Transfer in Multiple Scattering and Emitting Layered Media, Applied Optics, 27, 2502–2509, https://doi.org/10.1364/AO.27.002502, 1988.

Stephens, G. L.: Radiation Profiles in Extended Water Clouds. II: Parameterization Schemes, Journal of the Atmospheric Sciences, https://doi.org/https://doi.org/10.1175/1520-0469(1978)035<2123:RPIEWC>2.0.CO;2, 1978.

Toll, V., Christensen, M., Quaas, J., and Bellouin, N.: Weak Average Liquid-Cloud-Water Response to Anthropogenic Aerosols, Nature, 572, 51–55, https://doi.org/10.1038/s41586-019-1423-9, 2019.

Trenberth, K. E., Fasullo, J. T., and Balmaseda, M. A.: Earth's Energy Imbalance, Journal of Climate, https://doi.org/10.1175/JCLI-D-13-00294.1, 2014.

Turner, D. D., Clough, S. A., Liljegren, J. C., Clothiaux, E. E., Cady-Pereira, K. E., and Gaustad, K. L.: Retrieving Liquid Water Path and Precipitable Water Vapor From the Atmospheric Radiation Measurement (ARM) Microwave Radiometers, IEEE Transactions on Geoscience and Remote Sensing, 45, 3680–3690, https://doi.org/10.1109/TGRS.2007.903703, 2007.

Twomey, S.: Pollution and the Planetary Albedo, Atmospheric Environment (1967), 8, 1251–1256, https://doi.org/10.1016/0004-6981(74)90004-3, 1974.

Twomey, S.: The Influence of Pollution on the Shortwave Albedo of Clouds, Journal of the Atmospheric Sciences, 1977.

Uin, J.: Nephelometer Instrument Handbook, Tech. Rep. DOE/SC-ARM-TR-165, U.S. Department of Energy, Atmospheric Measurement user facility, Richland, Washington, 2024.

Uin, J. and Enekwizu, O.: Cloud Condensation Nuclei Particle Counter Instrument Handbook, Tech. Rep. DOE/SCARM-TR-168, U.S. Department of Energy, Atmospheric Measurement user facility, Richland, Washington, 2024.

Uin, J., Aiken, A. C., Dubey, M. K., Kuang, C., Pekour, M., Salwen, C., Sedlacek, A. J., Senum, G., Smith, S., Wang, J., Watson, T. B., and Springston, S. R.: Atmospheric Radiation Measurement (ARM) Aerosol Observing Systems (AOS) for Surface-Based In Situ Atmospheric Aerosol and Trace Gas Measurements, Journal of Atmospheric and Oceanic Technology, 36, 2429–2447, https://doi.org/10.1175/JTECH-D-19-0077.1, 2019.

Wall, C. J., Storelvmo, T., and Possner, A.: Global Observations of Aerosol Indirect Effects from Marine Liquid Clouds, Atmospheric Chemistry and Physics, 23, 13 125–13 141, https://doi.org/10.5194/acp-23-13125-2023, 2023.

Wang, M., Su, J., Xu, Y., Han, X., Peng, N., and Ge, J.: Radiative Contributions of Different Cloud Types to Regional Energy Budget over the SACOL Site, Climate Dynamics, 61, 1697–1715, https://doi.org/10.1007/s00382-022-06651-0, 2023.

Wang, Y., Li, J., Fang, F., Zhang, P., He, J., Pöhlker, M. L., Henning, S., Tang, C., Jia, H., Wang, Y., Jian, B., Shi, J., and Huang, J.: In-Situ Observations Reveal Weak Hygroscopicity in the Southern Tibetan Plateau: Implications for Aerosol Activation and Indirect Effects, npj Climate and Atmospheric Science, 7, 1–11, https://doi.org/10.1038/s41612-024-00629-x, 2024.

Watson, T. B.: Aerosol Chemical Speciation Monitor (ACSM) Instrument Handbook, Tech. Rep. DOE/SC-ARM–TR-196, 1375336, DOE-ARM, https://doi.org/10.2172/1375336, 2017.

Wei, X., Chang, N.-B., Bai, K., and Gao, W.: Satellite Remote Sensing of Aerosol Optical Depth: Advances, Challenges, and Perspectives, Critical Reviews in Environmental Science and Technology, 50, 1640–1725, https://doi.org/10.1080/10643389.2019.1665944, 2020.

Wendisch, M., Pöschl, U., Andreae, M. O., Machado, L. A. T., Albrecht, R., Schlager, H., Rosenfeld, D., Martin, S. T., Abdelmonem, A., Afchine, A., Araùjo, A. C., Artaxo, P., Aufmhoff, H., Barbosa, H. M. J., Borrmann, S., Braga, R., Buchholz, B., Cecchini, M. A., Costa, A., Curtius, J., Dollner, M., Dorf, M., Dreiling, V., Ebert, V., Ehrlich, A., Ewald, F., Fisch, G., Fix, A., Frank, F., Fütterer, D., Heckl, C., Heidelberg, F., Hüneke, T., Jäkel, E., Järvinen, E., Jurkat, T., Kanter, S., Kästner, U., Kenntner, M., Kesselmeier, J., Klimach, T., Knecht, M., Kohl, R., Kölling, T., Krämer, M., Krüger, M., Krisna, T. C., Lavric, J. V., Longo, K., Mahnke, C., Manzi, A. O., Mayer, B., Mertes, S., Minikin, A., Molleker, S., Münch, S., Nillius, B., Pfeilsticker, K., Pöhlker, C., Roiger, A., Rose, D., Rosenow, D., Sauer, D., Schnaiter, M., Schneider, J., Schulz, C., de Souza, R. A. F., Spanu, A., Stock, P., Vila, D., Voigt, C., Walser, A., Walter, D., Weigel, R., Weinzierl, B., Werner, F., Yamasoe, M. A., Ziereis, H., Zinner, T., and Zöger, M.: ACRIDICON–CHUVA Campaign: Studying Tropical Deep Convective Clouds and Precipitation over Amazonia Using the New German Research Aircraft HALO, Bulletin of the American Meteorological Society, 97, 1885–1908, https://doi.org/10.1175/BAMS-D-14-00255.1, 2016.

Zhao, C. and Garrett, T. J.: Effects of Arctic Haze on Surface Cloud Radiative Forcing, Geophysical Research Letters, 42, 557–564, https://doi.org/10.1002/2014GL062015, 2015.